Received: 8 February 2020 | Revised: 11 April 2020 | Accepted: 4 May 2020

DOI: 10.1111/bre.12466

ORIGINAL ARTICLE

Basin Research | IAS EAGE | WILEY

Signatures of tectonic-climatic interaction during the Late Cenozoic orogenesis along the northern Chinese Tian Shan

Xudong Zhao[1] | **Huiping Zhang**[1] | **Honghua Lv**[2] | **Yuanyuan Lü**[3] | **Xuemei Li**[1] | **Kang Liu**[1] | **Jiawei Zhang**[1] | **Jianguo Xiong**[1]

[1]State Key Laboratory of Earthquake Dynamics, Institute of Geology, China Earthquake Administration, Beijing, China

[2]Key Laboratory of Geographic Information Science of Ministry of Education, School of Geographic Sciences, East China Normal University, Shanghai, China

[3]Institute of Mineral Resources, Chinese Academy of Geological Sciences, Beijing, China

Correspondence
Huiping Zhang, State Key Laboratory of Earthquake Dynamics, Institute of Geology, China Earthquake Administration, Beijing 10029, China.
Email: huiping@ies.ac.cn

Funding information
National Natural Science Foundation of China, Grant/Award Number: 41622204 and 41761144071; Second Tibetan Plateau Scientific Expedition and Research

Abstract

The Chinese Tian Shan is one of the most actively growing orogenic ranges in Central Asia. The Late Miocene-Quaternary landscape evolution of northern Tian Shan has been significantly driven by the interaction between tectonic deformations and climate change, further modulated by the erosion of the upstream bedrocks and deposition into the downstream basins. In this study, only the accessible Kuitun River drainage basin in northern Tian Shan was considered, and detrital zircon geochronology and heavy minerals were analyzed to investigate the signature of the driving forces for Miocene sedimentation in northern Tian Shan. This study first confirmed a previously recognized tectonic uplift at ca. 7.0 Ma and further revealed that the basin sediments were mainly derived from the present glacier-covered ridge-crest regions during 3.3–2.5 Ma. It is suggested Late-Pliocene to Early Pleistocene sedimentation was likely a response to the onset of the northern hemispheric glaciation. Although complicated, this study highlights that the tectonic-climatic interaction during the Late Cenozoic orogenesis can be discriminated in the northern Chinese Tian Shan.

KEYWORDS

Chinese Tian Shan, landscape evolution, miocene sedimentation, tectonic-climatic interaction

1 | INTRODUCTION

Numerous studies have shown that tectonic activity and climate fluctuations can drive or influence the topographic evolution of mountain ranges (DeCelles & Mitra, 1995; Searle, Avouac, Elliott, & Dyck, 2017; Whipple, 2009); however, the method to unravel the process and tectonic-climatic interactions remains a challenge. Tectonic deformations or crustal shortening can lead to surface uplift and consequent growth of topographic relief (Yin, Dang, Zhang, Chen, & McRivette, 2008), followed by the growth of the gradient and stream power of river channels. However, increased precipitation and glaciation can also enhance surface erosion rates and thereby deliver more sediment into the flanking basins (Angela, Jacob, Daniel, & Andrea, 2018; Berger et al., 2008; Zhang, Molnar, & Downs, 2001). For instance, an increasing number of studies have indicated that the Late Cenozoic global cooling appears to enhance surface erosion of orogenic belt highlands (Berger et al., 2008; Herman et al., 2013; Thomson et al., 2010; Whipple, 2009), leading to increased sediment accumulation rates (Charreau et al., 2011; Molnar, 2004; Zhang et al., 2001), and a distinct changes to the provenance signal (Angela et al., 2018; Sun, An, Clemens, Bloemendal, & Vandenberghe, 2010; Zhang et al., 2018). Sedimentary basin sequences are direct products of tectonic deformation and climatic variation, that bridge the basin-filling and

The peer review history for this article is available at https://publons.com/publon/10.1111/bre.12466

orogenesis (Dadson et al., 2003; Litty, Lanari, Burn, & Schlunegger, 2017). Therefore, the sedimentological records of terrestrial deposits can provide exceptional clues to understand the evolutionary history of sedimentary basin-orogenic belt systems, and to understand tectonic-climatic interaction during the process of orogenesis (Angela et al., 2018; Sun, Zhu, & Bowler, 2004; Wei et al., 2018).

The Chinese Tian Shan is one of the most active orogenic ranges in Central Asia (Lu et al., 2019). Adjacent foreland basins collected and preserved continuous Late Cenozoic deposits, including the uppermost Xiyu conglomerate (Charreau et al., 2009; Sun et al., 2004). These basin sediments around the high central Asia were a topic of argument, either due to tectonic uplift (Charreau et al., 2009; Lu, Burbank, Li, & Liu, 2010), or due to enhanced Pleistocene glaciation (Charreau et al., 2011; Zhang et al., 2001). Because the provenance characteristics of these Neogene sediments are closely related to the lithological composition of the northern Tian Shan, clarifying the sediment provenance and its supply sources is key to revealing the interaction between climate and tectonics during the Late Cenozoic orogenesisalong the northern Chinese Tian Shan. This study presents detailed sedimentological information and reports 1,632 new U-Pb ages of detrital zircons (DZ) and 17 heavy mineral samples within the Kuitun River drainage basin. The goal of the study is to characterize the provenance of the Late Cenozoic deposits and to reconcile the driving forces by tectonics or climate change, or their interaction. Additional discussions are presented in relation to its significance to understand the Late Cenozoic landscape evolution of the globally glaciated uplifting orogens.

Highlights

- Tectonic uplift was the principal factor driving the change in sediment supply at ca. 7.0 Ma.
- The shift in sedimentation at ca. 3.3–2.5 Ma was mostly occurred by the contemporaneous glaciation.
- The growth of the northern Tian Shan during the Pleistocene might obey critical-taper wedge theory.

2 | GEOLOGICAL SETTING

The Chinese Tian Shan is bordered by the Tarim Basin to the south and the Junggar Basin to the north (Figure 1a), with an average elevation of ~2500 m and a summit > 7000 m (Charreau, Avouac, Chen, Dominguez, & Gilder, 2008). The widespread modern glaciers, as well as well-preserved Quaternary glacial landforms and sediments, suggest that glacier-driven erosion has significantly affected the surface process (Zhao, Liu, He, & Song, 2009). Although previous studies have provided a framework of glacial chronology range from 459.7 ± 46 to 7.3 ± 0.8 ka in the Tian Shan region (Zhao et al., 2009; Zhao, Zhou, He, Ye, & Liu, 2006), the Early Pleistocene glaciation in the northern Tian Shan also indicates by glacial moraine formation (Zhang, 1985).

The paleo-Tian Shan Range began during the Late Paleozoic, following the closure of the paleo-Asian ocean (Windley, Allen, Zhang, Zhao, & Wang, 1990; Yin et al., 1998). Correspondingly, the northern Tian Shan is characterized by Late Devonian-Early Carboniferous magmatic rocks in response to the collision between the Yili and Junggar terranes; post-collisional granitoids were formed from the Late Carboniferous to the Permian (Han et al., 2010; Zhang et al., 2015). These Hercynian igneous rocks extending SE-NW along the northern margin of Yili Block are also called Borohoro plutons (Wang, Shu, et al., 2007). Subsequent tectonic events occurred during the Mesozoic that were associated with several accretion-collision events around the Tian Shan region (Yang, Song, & He, 2015). As a result, an extensive low-relief erosional surface was developed in the Late Jurassic, altered during the Late Cretaceous, and finally beveled during the Early Cenozoic (Gillespie et al., 2017; Jolivet et al., 2018; Sobel, Chen, & Heermance, 2006). The lack of Early Paleogene ages from the low-temperature thermochronology data northern Tian Shan and the occurrence of several meters-thick Palaeogene calcareous paleosols, in the basins surrounding the range, together imply a semi-arid climate, low subsidence rate, and no significant tectonic uplift at that time (Jolivet et al., 2018; Yin et al., 2017). Thermochronology studies have indicated that the strong deformation in the Tian Shan piedmont was initiated during the Early Miocene (Hendrix, Dumitru, & Graham, 1994; Sobel et al., 2006), consistent with the timing of provenance change (Chen, Fang, Song, & Meng, 2012; Xiang et al., 2019). During the Late Miocene-Early Pleistocene, renewed compressive deformation and glaciation erosion in the Tian Shan region were inferred by structural analysis (Charreau et al., 2008; Lu et al., 2010, 2015; Sun, Li, Zhang, & Fu, 2009), ^{10}Be-based paleo-erosion rates (Charreau et al., 2011) and low-temperature thermochronology (Yin et al., 2017; Yuan et al., 2004). Although the interactions between tectonics, climate, and surface processes during mountain building are complex, few reported cases are available to understand this concept. The northern Tian Shan is dominated by a frontal thrust fault (F_f), a middle thrust fault (F_m), and a back thrust fault (F_b) from north to south (Figure 1b). Within its foreland, at least three E-W or W-NW trending fold-and-thrust belts formed from the Early Miocene to Quaternary, namely the Piedmont fold-and-thrust belt, the Huoerguos-Manas-Tugulu fold-and-thrust belt, and the Dushanzi-Halaande-Anjihai fold-and-thrust belt (Charreau et al., 2008; Hendrix et al., 1994; Lu

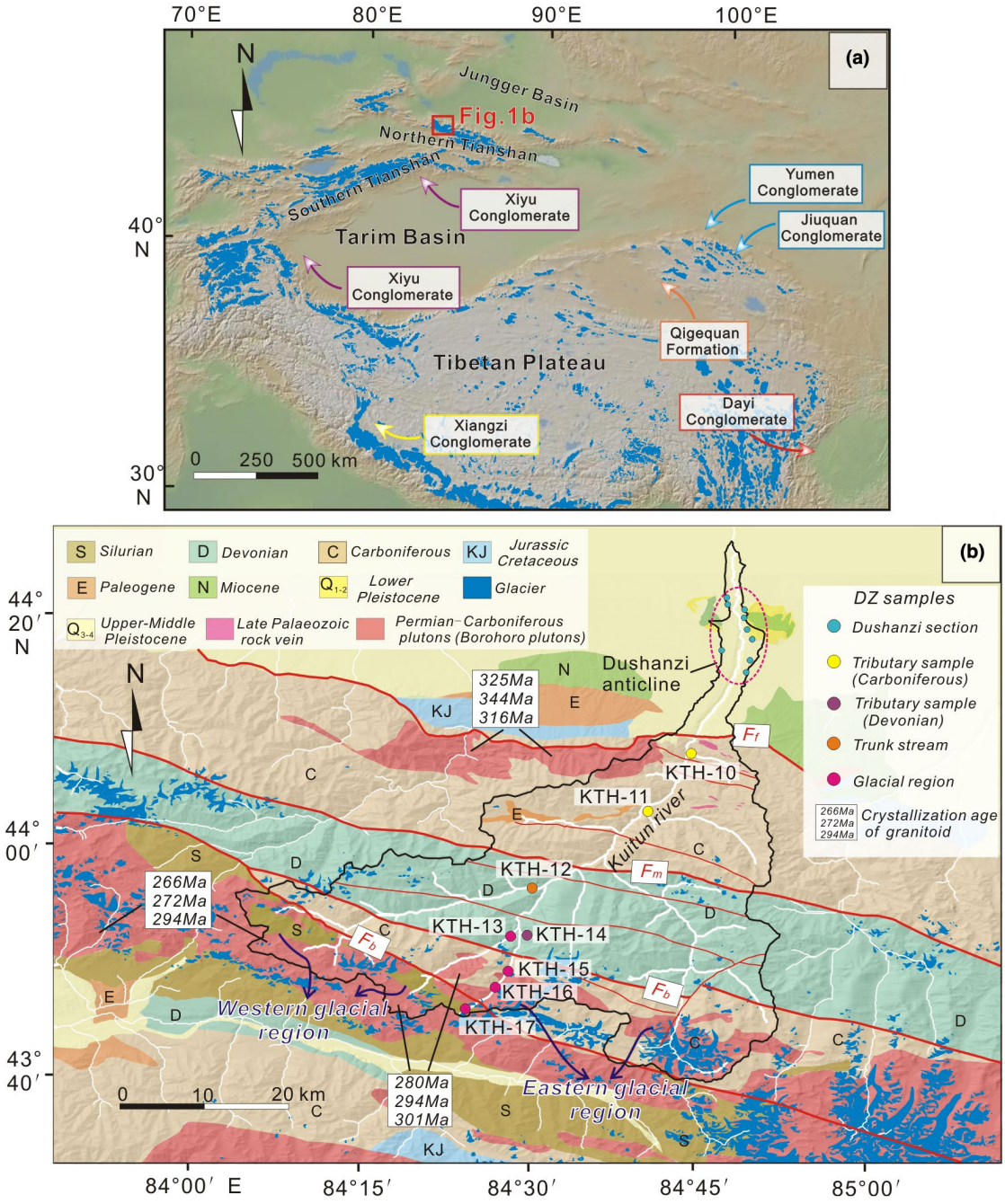

FIGURE 1 (a) Topographic map of Central Asia and the Tibetan Plateau. Pale blue polygons are mapped Late Pleistocene glacier extents (Li, Zhou, & Pan, 1991; Pfeffer et al., 2014). The coloured arrows indicate the sites of the Quaternary coarse-grained clastic sediments around glacier-covered regions. The red box corresponds to the fragment of the Kuitun River catchment showed in Figure 1b. (b) Geological map and sample locations of the Kuitun River catchment area. The crystallization ages of granite are from Wang, Shu, et al. (2007) and Han et al. (2010). F_f = The frontal thrust fault; F_m = The middle thrust fault; F_b, The back thrust fault. The faults with thick line-weights represent major thrust faults in the Northern Tianshan Range

et al., 2010; Sun et al., 2004). No significant changes in the deformation across the Tian Shan and its foreland basins were suggested after at least the Late Pleistocene (Lu et al., 2019).

A series of subparallel northward-draining rivers that originated from the highland of northern Tian Shan incised the foreland basin fills and exposed well-developed Neogene sedimentary sequences (Lu et al., 2010, 2015; Sun et al., 2004). Among them is the ~100 km long Kuitun River with a drainage basin area of ~2030 km^2 (Figure 1b) and a mean elevation of ~1500 m. The headwater area currently covered by glaciers, is characterized by low relief topography (slope < 30°), with a downstream slope increases to 30–40°. The present uplifted catchment range has exposed various bedrock units: Devonian to Carboniferous sedimentary rocks

in the lower and middle catchment reaches that are intruded by the Late Paleozoic intermediate-basic dyke swarms; and Late Carboniferous-Early Permian A-type and I-type granitoids and limited Silurian sandstone in the upper reaches (Figure 1b). The ages (309–266 Ma) of these Late Paleozoic granitoids are from Wang, Wyman et al. (2007) and Zhu, Zhang, Gu, Guo, and Zhou (2005).

3 | Methods

3.1 | Sedimentology

In this study, the sedimentological investigations from upper Miocene to Quaternary stratigraphic succession at the Dushanzi section along the Kuitun River are presented first (Figure 2). The depositional ages and stratigraphic division scheme of this section were adapted from the magnetostratigraphy study of Sun et al. (2004; Figure 2b). The sedimentary analysis of lithology, colour, texture, primary sedimentary structure, and vertical succession, the facies characteristics, and paleodepositional environments were provided and discussed along with detailed heavy mineral results and detrital zircon spectral data. The lithofacies analysis followed the criteria of Miall (1996; Table 1).

3.2 | Heavy mineral analysis

Seventeen sandstone samples were collected for heavy mineral analysis and detrital zircon U-Pb dating, including nine

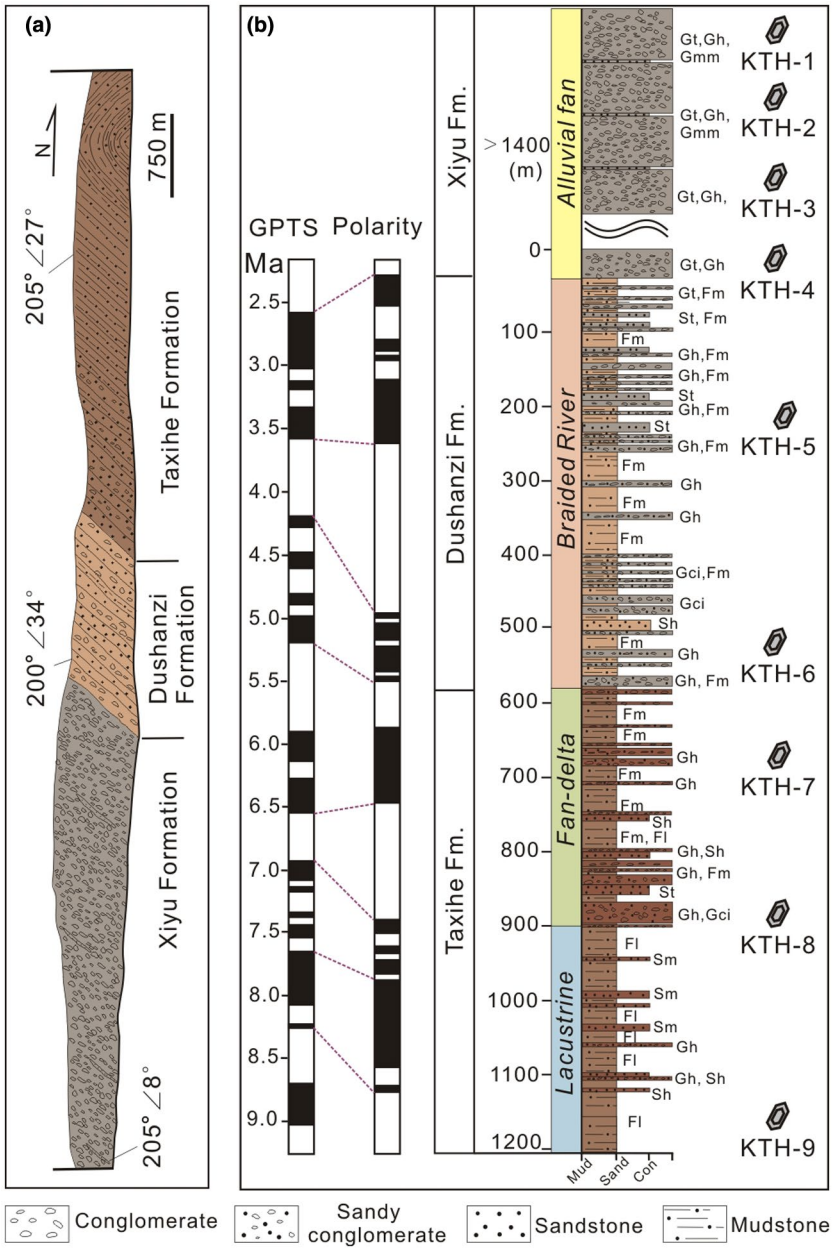

FIGURE 2 (a) Geologic cross-section across the Dushanzi anticline exposed by the Kuitun River (after Sun et al., 2004). Dips are nearly consistent from the Taxihe Formation to the lower Xiyu Formation, but shallow upward thereafter. (b) Stratigraphy and magnetostratigraphy of Late Miocene to Quaternary sedimentary sequences along the Dushanzi section (after Sun et al., 2004), with schematic heavy mineral and detrital zircon sample locations. The magnetostratigraphy of the section was correlated to GPTS (CK1995). The location of the Dushanzi section is indicated in Figure 1b

TABLE 1 Lithofacies and interpretations used in this study

Code	Description	Interpretation
Fl	Reddish/greenish fine-grained sandstone to siltstone, mudstone with millimetre-scale rhythmic laminations	Suspension-settling in ponds and lakes
Fm	Massive, very fine-grained sandstone to siltstone, mudstone	Suspension settling in the lake and overbank deposits
Sm	Massive fine- to coarse-grained sandstone	Sandy mudflows and suspension settling in the lake and overbank deposits
St	Fine- to very coarse-grained sandstone with trough cross-stratification	Migration of large 3D ripples (dunes) under moderately powerful unidirectional flows in large channels
Sh	Fine- to coarse-grained sandstone with plane-parallel lamination	Upper plane bed conditions under unidirectional flows, either strong or very shallow
Sr	Fine- to medium-grained sandstone with small, 2D and 3D current ripples	Migration of small 2D and 3D ripples under weak, unidirectional flows in shallow channels
Gt	Pebble to cobble conglomerate and sandy conglomerate, stratified, trough cross-beds	Minor channel fills
Gh	Pebble to cobble conglomerate and sandy conglomerate, clast-supported, crudely, bedded gravel with horizontal bedding and imbrication	Longitudinal bedforms, lag deposits, sieve deposits
Gmm	Massive, matrix-supported pebble to cobble conglomerate, poorly sorted, disorganized, unstratified	Deposition by matrix-rich debris flow under the braided river channel
Gci	Pebble to cobble conglomerate, clast-supported, horizontally stratified, imbricated, poorly sorted	Deposition from shallow traction currents in longitudinal bars and gravel sheets

Note: Modified after Miall (1996).

from the Dushanzi section, two from a tributary draining the Carboniferous strata, one from a tributary draining the Devonian strata, three from the eastern glacier-covered region, and two modern riverbed samples that represent the western glacier-covered region source (Figure 1b). The sample ages from the Dushanzi section are about 8.5, 6.8, 5.8, 4.6, 3.3, 2.5, 1.9, 1.4, and 0.8 Ma, as reported by Sun et al. (2004; Figure 2).

Heavy minerals are defined as components with a density of more than 2.89 g/cm^3 in sedimentary rocks, which are commonly applied as provenance tracers (Morton & Hallsworth, 2007). Samples weighing 2–4 kg of medium to coarse-grained sandstone were collected. To extract heavy minerals, a bulk sample was crushed and clay and silt particles were removed, where only material within the 0.063–0.212 mm grain-size fraction were selected. They were washed with hydrogen peroxide and dilute hydrochloric acid. The extracted minerals were separated with a heavy liquid of tribromomethane and identified under a microscope. To show similarities/differences of heavy mineral assemblages of individual sandstone samples, principal component analysis (PCA) for heavy mineral assemblages were combined (Hammer, Harper, & Ryan, 2001). Principal component analysis (PCA) is a robust and flexible statistical procedure, which uses orthogonal transformation of the observation value of a group of possibly related variables into a group of linearly uncorrelated variables called principal component (PCs). This method can reduce the dimension of a data set composed of many related variables, while preserving the changes in the data set as much as possible. Generally, PCV1 represents the most significant variable, while PCV2 represents the second most significant variable in the PCA map. The calculation was completed using the free software package PAST-Paleontological Statistics (Hammer et al., 2001).

3.3 | Detrital zircon geochronology

Detrital zircon provenance tracing has become increasingly useful as a proxy for unraveling the source-to-sink relationships between sedimentary basins and adjacent potential source regions (e.g. Angela et al., 2018; Cheng et al., 2019; Gehrels et al., 2011; Litty et al., 2017). Zircon target preparation, cathodoluminescence imaging (CL), and U-Pb dating were completed at the State Key Laboratory of Earthquake Dynamics, Institute of Geology, China Earthquake Administration. Sandstone samples were crushed to 80–100 mesh and at least 2,000 detrital zircon grains were selected for each sample by conventional flotation and magnetic separation methods. In this study, 300 zircon grains were randomly selected to adhere to double-sided adhesive and were poured into the laser sample target with epoxy resin. After polishing, the zircon samples were photographed using reflected light and CL to select the appropriate zircon grains and laser denudation locations. Laser ablation inductively coupled plasma mass spectrometry (LA-ICP-MS) was employed, using an Agilent 7900 produced by Agilent Technologies with a 193nm excimer laser-ablation system from Resolution M50-LR, for ICP-MS. All samples were ablated by a 28 μm laser beam diameter, a frequency of 10 Hz, and with a laser energy density of 4.0 J/cm^2. The mentioned the age of 91,500 was used as the monitoring standard; the element content was determined by NIST610 as the external standard, and ^{29}Si as the internal standard, once every five measuring points. The analytical procedures have been detailed by Yuan et al. (2004). The data were processed using the Glitter 4.0 software, while the common lead correction method followed Andersen (2002). A <10% discordance filter was applied to the generated data. For detrital zircon grains older than 1000 Ma, the ^{207}Pb/^{206}Pb apparent age was adopted due to the existence of a large number of radiogenic Pb, while for those younger than 1000 Ma, the more reliable ^{206}Pb/^{238}U apparent age was adopted due to the lower content of measurable radiogenic Pb (Sircombe, 1999).

To adequately show similarities/differences of the zircon U-Pb age distributions of individual sandstone samples and extract mixing proportions of source rock contributions, this study combines multidimensional scaling analysis (MDS) and the Kolmogorov-Smirnoff (K–S) test for zircon U-Pb ages (Vermeesch., 2013; Wang et al., 2016). MDS is a standard statistical technique and allows a quick and effective comparison between U-Pb ages of a sediment sample and mixed samples from potential source areas. This method makes abstracts the data and may not always represent all the details of complex datasets. Given a table of pairwise 'dissimilarities' between samples, MDS produces a 'map' of points on which 'similar' samples cluster closely together, and 'dissimilar' samples plot far apart (Vermeesch., 2013). The calculations were performed using the mdscale function of the Statistics Toolbox in Matlab (Vermeesch., 2013). The K–S test analysis is a simple quantitative tool that provides the dissimilarity between samples. Two age distributions returned high p values ($p > .05$) from the K–S test, which implies that the two age spectra are nearly identical, whereas p values of 0 have virtual certainty of different parent populations. For details about this method, we refer readers to Wang et al. (2016).

4 | RESULTS

4.1 | Stratigraphy and sedimentology

At the Dushanzi section, the Late Cenozoic succession can be subdivided into three stratigraphic units from oldest to youngest: the Taxihe, Dushanzi and Xiyu formations (Figure 2a). The stratigraphy of the most fundamental lithofacies (assemblages) are described below briefly (Table 1).

The first ~300 m of the Taxihe Formation (ca. 8.7–7.0 Ma) is predominantly by greenish to reddish siltstone and mudstone with several gray to greenish coarse-grained to gravelly sandstone interlayers (Sm, Sh, Gh; Sun et al., 2004). Some centimeter- to decimeter scale rhythmic laminations and small-scale ripple marks can be observed in these finer deposits (Fl; RSGXJR (Regional stratigraphic table compilation group of Xinjiang Uygur Autonomous Region) 1981), which mostly formed in quiet-water environments (Miall, 2016). Therefore, this set of deposits were interpreted to have accumulated in a lacustrine system. The upper part of the Taxihe Formation (ca. 7–5.3 Ma) is composed of variably colored sandy conglomerate to conglomerate, fine- to coarse-grained sandstone, siltstone, and mudstone with abundant preserved plant material (RSGXJR 1981). Mudstones and siltstones are greenish to reddish in colour, centimeters to meters thick, and laterally continuous over hundreds of meters (this study; RSGXJR 1981). Various scales of cross-bedding and erosional contacts of the coarse-grained to gravelly sandstone, and lenticular sandstone body reveal that many beds were deposited by relatively energetic currents. The characteristic of alternating sandy conglomerates, sandstone, and mudstone to siltstone may document a subaerial delta-plain with distributary channels. Coupled with the observation of the coarsening-upward nature of most deltaic deposits (Miall, 2016), this unit was interpreted as the deposits of delta, as suggested by Sun et al. (2004).

The Dushanzi Formation (ca. 5.3–2.6 Ma) consists mainly of brownish or gray-yellowish sandstone, siltstone as well as an interbedded pebble or cobble conglomerate layers (RSGXJR, 1981; Sun et al., 2004; Figure 3c, 3d). Upward-fining successions and medium to small scales of cross-beddings can be observed within sandy conglomerate to sandstone beds with basal granule lags (St), which were regarded as the products of channel migration and filling processes (Miall, 1996).

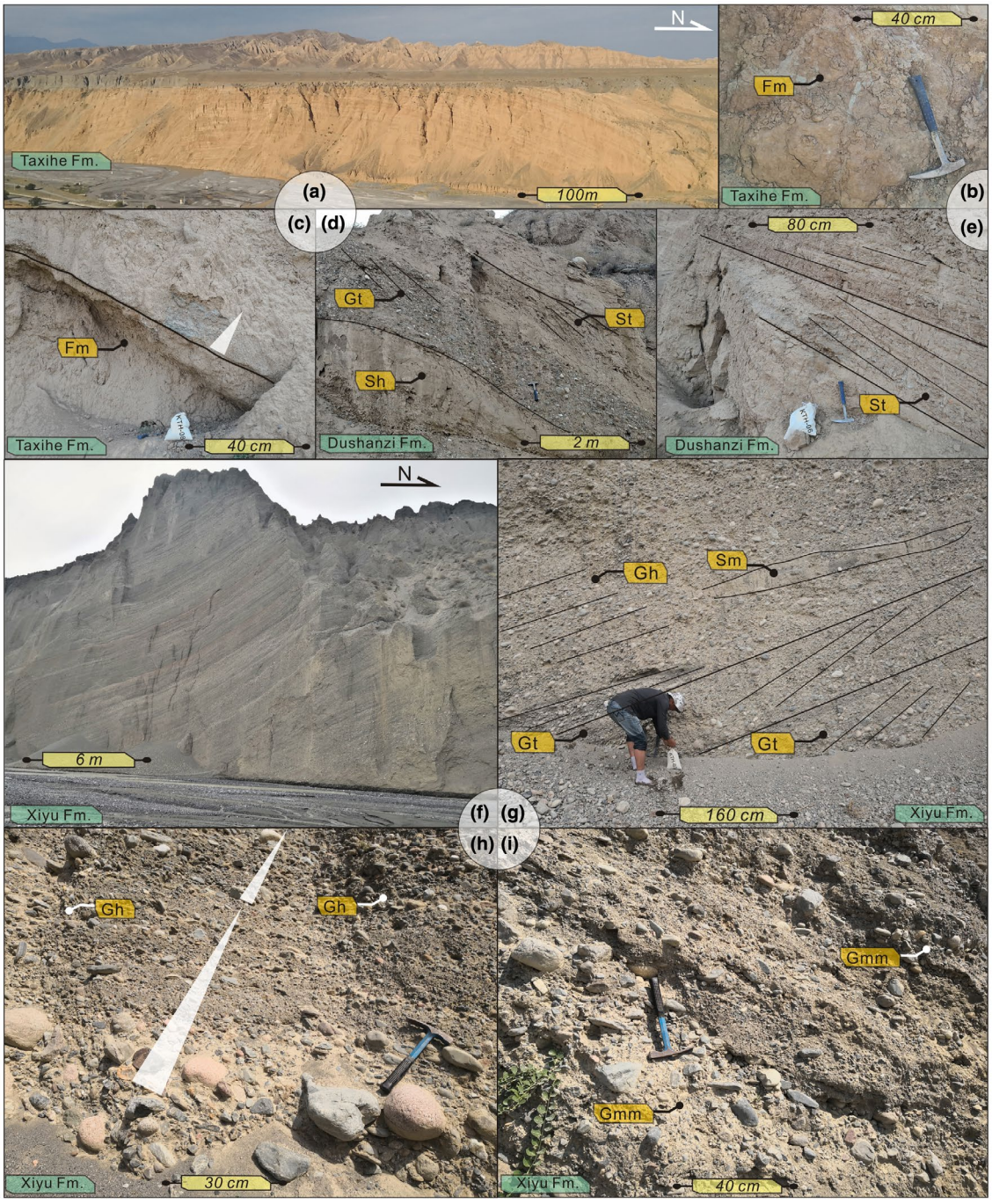

FIGURE 3 Photographs showing the sedimentary characteristics in the Dushanzi section. (a) Panoramic photograph for the Dushanzi anticline core, showing the lower parts of the Taxihe Formation. (b) Massive fine-grained sandstone, siltstone, and mudstone indicates that sediment settled out of suspension in still water. (c) Base of channel-fill with scouring surface, normally graded, coarse-grained to gravelly sandstone. (d) Medium-grained to gravelly sandstones with meter-thick, planar cross-stratified pebble and cobble conglomerates interbeds. (e) Decimeter- to meter- thick, stacked medium-grained to gravelly well-sorted, sandstones with cross and parallel lamination. (f) Horizontal to sub-horizontal bedded, and clast-supported conglomerates. Individual beds are typically several decimeters thick, with multistory units reaching several meters in thickness. (g) Clast-supported, subangular to subrounded, crudely stratified pebbles to cobbles with decimeter-thick lenticular sandstones, represent flood channel deposits on the surface of an alluvial fan system. (h) Clast-supported conglomerates with crude horizontal and planar cross-stratification. Note an upward decrease in the clast size. (i) Disorganized, angular to sub-angular, and matrix-supported conglomerates, reflect the formation of these deposits by the process of high-strength debris flows

The conglomerate beds are typically clast-supported, with crude horizontal stratification (Gh). Individual conglomerate beds are typically several meters thick, with multistory units reaching tens of meters in thickness. Clasts within the conglomerate beds are 5–15 cm in size, poorly sorted, and sub-rounded to subangular (Sun et al., 2004). Massive siltstones

and mudstones pinch out laterally, and extend over tens of meters (Fm), which may be from the suspension load of rivers, representing the deposits from standing pools of water during low-stage channel abandonment (Miall, 2006). The ensemble of these observations suggests that these clastic materials were deposited in a braided river system, which was probably characterized by a relatively active valley with several or many component channels of varying sinuosity.

The Xiyu Formation (<2.6 Ma) is more than 1400 m in thickness and consists mainly of clast-supported pebble- to cobble-sized conglomerates, with matrix-supported pebble- to boulder conglomerates and meter- to decimeter-thick sandy lenticular interbeds. Clast-supported conglomerates laterally extend over several tens to hundreds of meters. Individual beds are typically several decimeters to meters thick, with multistory units reaching tens of meters in thickness. The conglomerates display crude horizontal stratification, trough cross-bedding, and upward-fining successions (Gt, Gh; this study; Charreau et al., 2005). Clasts are commonly imbricated. These observations suggest that the clast-supported conglomerates were deposited as channel fills and scours within an alluvial fan system (Miall, 1996). Matrix-supported conglomerates are generally 5–50 cm in size, poorly sorted and subrounded to subangular, and lacking distinct sedimentary flow structures (Gm; Sun et al., 2004). Beds of these lithofacies have sharp but nonerosional relationships with underlying beds. Thus, the transport and deposition of this matrix-supported conglomerates most likely occurred through debris flows and flash flood processes (Schlunegger, Norton, Delunel, Ehlers, & Madella, 2017). Overall, the dominance of clast-supported and partially imbricated fabric indicates that Kuitun River runoff was most likely perennial at that time.

4.2 | Heavy mineral assemblages

The heavy mineral suites of all samples consist mainly of sphene, ilmenite, magnetite, hematite, and zircon associated with a few leucoxene, apatite, hornblende, pyroxene, and garnet. In the Taxihe Formation samples (sample KTH-07 to sample KTH-09), the mean proportions of ilmenite, magnetite, sphene, zircon, and epidote are 27%, 31%, 6%, 9%, and 8%, respectively (Table S1). The proportions of rutile, hornblende, pyroxene, and anatase are negligible in most samples. In the Dushanzi Formation samples (samples KTH-05 and KTH-06), the proportions of most of the heavy mineral types are stable relative to the Taxihe Formation, only the epidote proportion of decreased slightly upsection.

Samples from the Xiyu Formation (sample KTH-01 to sample KTH-04) are dominated by hematite (5%–16%), zircon (10%–21%), magnetite (27%–28%), ilmenite (11%–17%), and epidote (6%). From the Dushanzi Formation to the Xiyu Formation samples (sample KTH-06 to sample KTH-01), the proportion of zircon and hematite gradually increases (from 4%, 5% in sample KTH-06 to 17%, 16% in sample KTH-04), while the total proportion of ilmenite decreases (from 42% in sample KTH-06 to 13% in sample KTH-04; Figure 4b; Table S1).

Among the tributaries draining the Devonian and Carboniferous strata, sample KTH-14 is dominated by ilmenite (35%) and magnetite (16%); samples KTH-10 and KTH-11 are dominated by magnetite (32%–33%) and hematite (10%–33%), and are marked by the unstable mineral pyroxene (21% in sample KTH-10). Contrastingly, the heavy mineral assemblages of the upper reaches were marked by garnet (2%–30%), epidote (3%–18%), and zircon (10%–19%) in the eastern region, by magnetite (27%–38%), ilmenite (17%–24%), and hornblende (4%–7%) in the western region, which are similar to those sampled in the Xiyu Formation (Table S1).

To compare the similarity or dissimilarity of heavy mineral assemblages, Principal component analysis (PCA) was used. All the heavy-mineral sample data are plotted on the PCV1 and PCV2 axes using the PAST software (Figure 5; Hammer et al., 2001). The PCA plot shows that the four samples from the Xiyu Formation plot closer to those from the upper reaches (the present-day glacier-covered regions), and are statistically different from the Dushanzi Formation samples.

4.3 | Zircon U-Pb geochronology results

In total, 1,632 concordant ages were obtained from 17 sandstone or modern riverbed samples. The zircon grains from all the samples show euhedral to abraded shapes with an average size ranging between 40 and 260 μm. Most of the zircon crystals display distinct oscillatory zoning on the CL images (Figure S1), indicating the predominance of magmatic zircon. The Th/U ratios vary from 0.12 to 1.55, again indicative of a largely magmatic origin (Hoskin & Black, 2000).

The zircon U-Pb ages of all samples are dominated by Paleozoic ages. In the Dushanzi section, DZ ages from the samples from the Taxihe and Dushanzi Formations range between 265 and 310 Ma (81%–91%), except for the bottom-most sample KTH-9. Samples from the Xiyu Formation show two zircon-age populations that are 265–290 Ma (29%–57%) and 290–360 Ma (33%–61%). In the uplifted range, the three diluvium samples (KTH-15, KTH-16, KTH-17) also display one major age interval at 265–310 Ma (48%–74%). Two samples from the modern riverbed of the upper reaches (KTH-12, KTH-13) show younger DZ age signatures of <290Ma (31%–72%). Samples from the tributaries draining the Devonian and Carboniferous strata (KTH-10, KTH-11, KTH-14) contain much higher proportions of

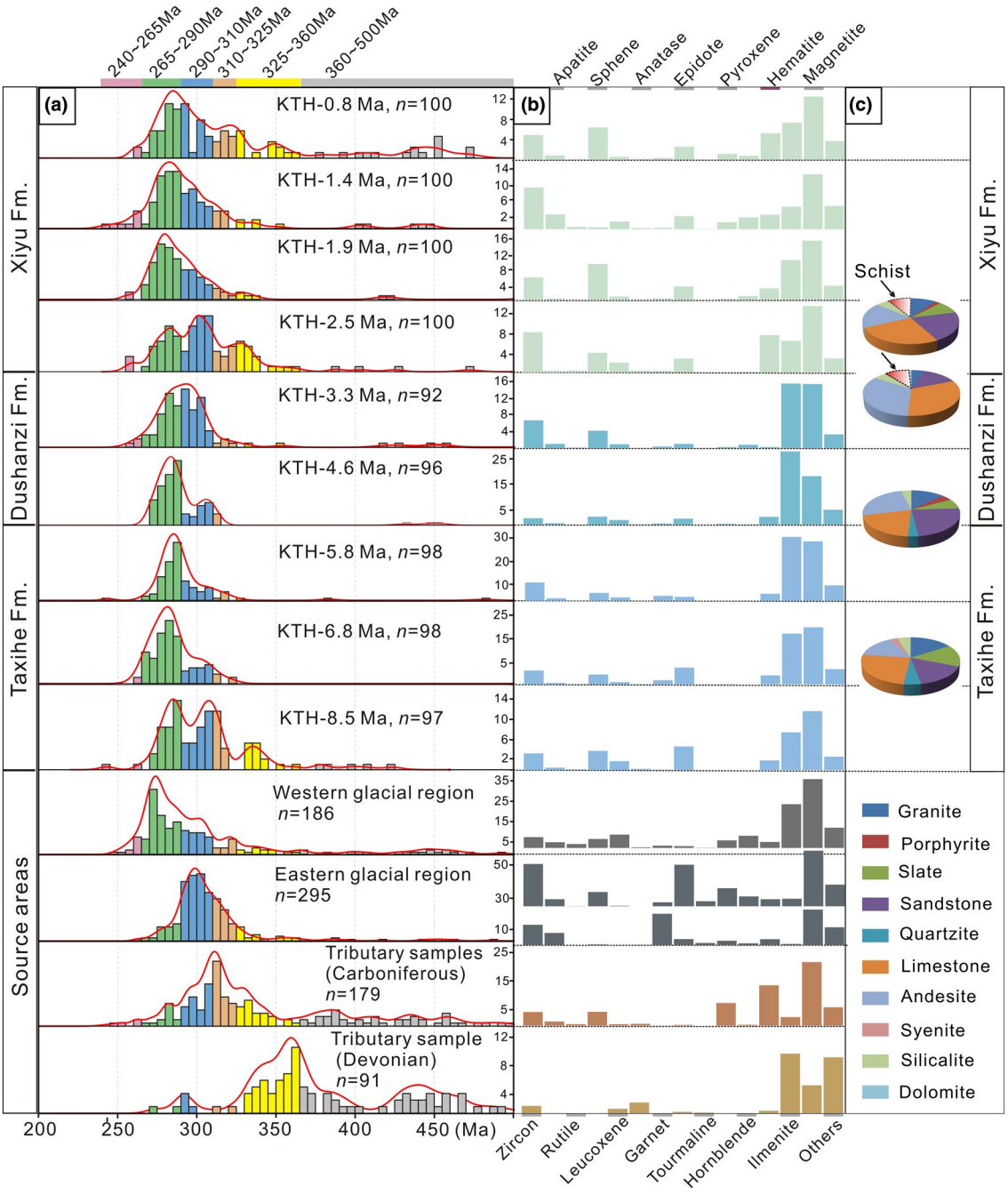

FIGURE 4 Composite plot of provenance data for samples, including (a) Combined histogram plots (coloured bars) and probability density functions (red lines) depicting the zircon U-Pb ages of samples from the Dushanzi section and potential source area. KTH-x Ma indicates the depositional age of the sandstone samples. The number of zircons is given on the vertical axis (right). (b) Heavy mineral assemblages. Each histogram represents one sample with different proportions of heavy mineral types. See Table S1 for complete results. (c) Percentage component pie chart of conglomerate clast compositions (after Sun et al., 2004)

pre-Permian aged zircons (ca. 80% U-Pb ages >310 Ma) than other samples from these source areas (Figure 4a, Table 2, Table S2). Detailed zircon U-Pb data from all samples are presented in Table 2 and Table S1.

The MDS map plots the similarities/dissimilarities among detrital samples representing source areas, the Taxihe and Dushanzi Formations deposits, and the Xiyu conglomerates. Consistent with the PCA of heavy minerals, the samples from the Xiyu Formation are close to the samples from the upper reaches. No similarity is observed between the samples from the Late Cenozoic and those from the tributaries draining the Devonian and Carboniferous, particularly with respect to the characteristic 360–500 Ma population ages of the Devonian and Carboniferous strata being absent in the Late Cenozoic deposits. From the K–S test, the sample KTH-09 (ca. 8.5 Ma) exhibits p values near

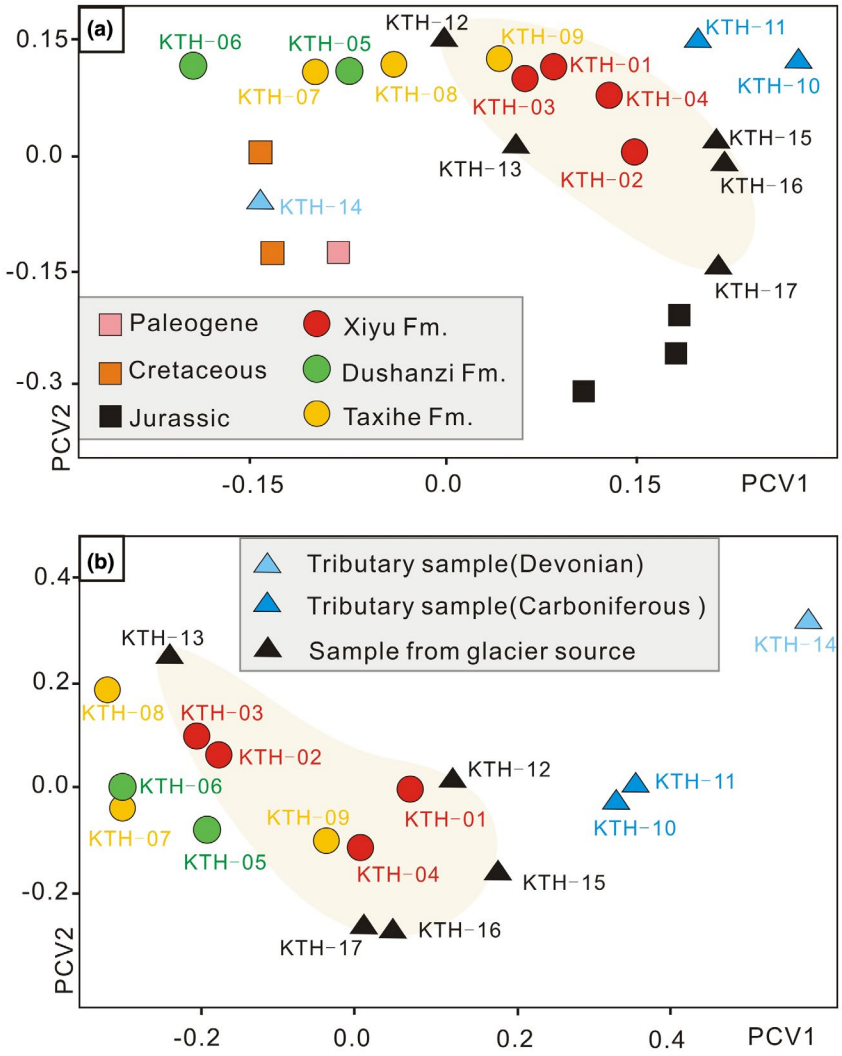

FIGURE 5 (a) Principal component analysis (PCA) of heavy mineral assemblages in the Kuitun River watershed. Plot shows dissimilarities between samples as a map where similar samples cluster and differing samples plot far apart. The red solid circles, green solid circles, and orange solid circles represent heavy mineral assemblages of the samples from Xiyu, Dushanzi and Taxihe Formations, respectively. The black solid triangles represent heavy mineral assemblages from the Permian-Carboniferous igneous rocks, while the blue solid triangles represent heavy mineral assemblages of the samples from the Devonian and Carboniferous drainage (the piedmont fold-thrust belt). The black solid squares, orange solid squares, and pink solid squares without names represent heavy mineral assemblages of Jurassic, Cretaceous and Paleogene samples collected from the adjacent area and data of these six samples are from Fang et al. (2006). (b) Multidimensional scaling (MDS) plot of age dataset from the Dushanzi section and modern fluvial (diluvium) systems in the Kuitun River watershed. Axes are in dimensionless 'K–S units' ($0 < KS < 1$), showing 'distance' between samples. PC1 and PC2 refer to the two principal components. Symbols are the same as those in Figure 5a. Note that heavy mineral assemblages and detrital zircon age distributions from Xiyu Formations (samples KTH-1 to KTH-4) are statistically similar to those of modern samples from the present-day glacier-covered regions (samples KTH-12 to KTH-13 and samples KTH-15 to KTH-17). See supplementary material for complete data

zero with the 6.8–3.3 samples, indicating that the dominant volume of zircons in the ca. 8.5 Ma sample are remarkably different than the 6.8–3.3 Ma samples (Table 3). The 6.8–3.3 Ma samples exhibit a high resemblance to the samples from the western glacial region, indicated by *p* values from .044 to .912, whereas the ca. 2.5–0.8 Ma samples present relatively high *P* values samples from the whole glacial region, but display zero *P* values compared with the samples from tributaries draining the Devonian and Carboniferous. This suggests a clear difference in the zircon age distribution patterns of the 6.8–3.3 Ma samples with post-2.5 Ma samples, also indicates the detrital zircons from the ca. 2.5–0.8 Ma strata are mostly derived from the uppermost reaches.

When considered concurrently, heavy-mineral assemblages and detrital zircon (DZ) ages of the Late Miocene to Quaternary samples from the Dushanzi section are generally similar to those from the current glacier-covered regions in the Kuitun River drainage area, but compare poorly with the samples from the tributaries draining

TABLE 2 Summary of major characteristics and corresponding statistical data for 17 detrital zircon samples

Formation/deposit type	Sample number	Detrital zircon age peaks (Ma)	Detrital zircon age range (Ma)	Percentage of the total effective grains					
				<265 Ma	265–290 Ma	290–310 Ma	310–325 Ma	325–360 Ma	>360 Ma
Xiyu Fm.	KTH-01	285, 321, 446	260–1736	3% (3)	29% (29)	22% (22)	13% (13)	12% (12)	21% (21)
Xiyu Fm.	KTH-02	284	241–856	8% (8)	47% (47)	27% (27)	8% (8)	4% (4)	6% (6)
Xiyu Fm.	KTH-03	280	256–1708	2% (2)	57% (57)	24% (24)	5% (5)	4% (4)	8% (8)
Xiyu Fm.	KTH-04	284, 301, 330	256–472	4% (4)	30% (30)	33% (33)	11% (11)	17% (17)	5% (5)
Dushanzi Fm.	KTH-05	293	257–1152	3% (3)	43% (39)	40% (37)	4% (4)	2% (2)	8% (7)
Dushanzi Fm.	KTH-06	285, 307	267–1754	0% (0)	67% (64)	24% (23)	3% (3)	0% (0)	6% (6)
Taxihe Fm.	KTH-07	284	244–1561	1% (1)	66% (64)	23% (22)	7% (6)	0% (0)	5% (5)
Taxihe Fm.	KTH-08	282	260–2250	2% (2)	72% (71)	19% (19)	5% (5)	0% (0)	2% (2)
Taxihe Fm.	KTH-09	285, 308, 335	243–424	2% (2)	33% (32)	33% (32)	12% (12)	14% (13)	6% (6)
Modern river sand	KTH-10	280, 312, 382, 438	245–1421	2% (2)	9% (8)	18% (16)	18% (16)	11% (10)	42% (36)
Modern river sand	KTH-11	310, 387, 459	253–2607	2% (2)	5% (5)	22% (20)	20% (18)	18% (17)	33% (30)
Modern river sand	KTH-12	272, 302, 447	265–1945	1% (1)	30% (27)	21% (19)	12% (11)	9% (8)	27% (24)
Modern river sand	KTH-13	274	249–2677	14% (13)	58% (56)	18% (17)	2% (2)	3% (3)	5% (5)
Modern river sand	KTH-14	358, 440, 292	274–3607	0% (0)	3% (2)	5% (4)	3% (2)	33% (29)	60% (54)
Deluvium	KTH-15	304	265–1551	1% (1)	10% (10)	38% (37)	20% (19)	10% (10)	21% (20)
Deluvium	KTH-16	300	262–1274	1% (1)	12% (12)	58% (57)	22% (21)	4% (4)	3% (3)
Deluvium	KTH-17	299	274–879	0% (0)	15% (15)	59% (59)	16% (16)	5% (5)	5% (5)

TABLE 3 *p* values for the K–S comparison of the isotopic ages of detrital zircons from the Kuitun River watershed

		Xiyu Fm.				Dushanzi Fm.		Taxihe Fm.			Western glacial region			Eastern glacial region						Tributaries draining Devonian-Carboniferous
Samples		**KTH-01**	**KTH-02**	**KTH-03**	**KTH-04**	**KTH-05**	**KTH-06**	**KTH-07**	**KTH-08**	**KTH-09**	**KTH-12**	**KTH-3**	**Borohoro plutons**	**KTH-15**	**KTH-16**	**KTH-17**	**KTH-10**	**KTH-11**	**KTH-14**	
Xiyu Fm.	KTH-01		*.001*	*.001*	**.064**	*.001*	*.000*	*.000*	*.000*	**.089**	**.934**	*.000*	*.002*	***.036***	*.003*	*.007*	*.002*	*.002*	*.000*	
	KTH-02	*.001*		**1.000**	*.019*	**.938**	**.860**	**.822**	**.145**	*.024*	*.001*	**.094**	**.339**	*.000*	*.000*	*.000*	*.000*	*.000*	*.000*	
	KTH-03	*.001*	**1.000**		*.004*	**.653**	**.968**	**.725**	**.372**	*.008*	*.000*	**.126**	**.396**	*.000*	*.000*	*.000*	*.000*	*.000*	*.000*	
	KTH-04	**.064**	*.019*	*.004*		*.011*	*.000*	*.000*	*.000*	**1.000**	***.032***	*.000*	*.017*	**.053**	**.146**	**.330**	*.000*	*.000*	*.000*	
Dushanzi Fm.	KTH-05	*.001*	**.938**	**.653**	*.011*		**.183**	**.278**	*.010*	*.014*	*.000*	*.005*	**.064**	*.000*	*.000*	*.001*	*.000*	*.000*	*.000*	
	KTH-06	*.000*	**.860**	**.968**	*.000*	**.183**		**.999**	**.422**	*.001*	*.000*	*.026*	**.166**	*.000*	*.000*	*.000*	*.000*	*.000*	*.000*	
Taxihe Fm.	KTH-07	*.000*	**.822**	**.725**	*.000*	**.278**	**.999**		**.085**	*.000*	*.000*	*.002*	***.044***	*.000*	*.000*	*.000*	*.000*	*.000*	*.000*	
	KTH-08	*.000*	**.145**	**.372**	*.000*	*.010*	**.422**	**.085**		*.000*	*.000*	**.859**	**.912**	*.000*	*.000*	*.000*	*.000*	*.000*	*.000*	
	KTH-09	**.089**	*.024*	*.008*	**1.000**	*.014*	*.001*	*.000*	*.000*		*.044*	*.000*	*.008*	*.022*	**.068**	**.172**	*.000*	*.000*	*.000*	
Western glacial region	KTH-12	**.934**	*.001*	*.000*	*.032*	*.000*	*.000*	*.000*	*.000*	*.044*		*.000*	*.001*	**.076**	*.001*	*.004*	*.015*	*.015*	*.000*	
	KTH-13	*.000*	**.094**	**.126**	*.000*	*.005*	*.026*	*.002*	**.859**	*.000*	*.000*		**.872**	*.000*	*.000*	*.000*	*.000*	*.000*	*.000*	
	Borohoro plutons	*.000*	**.886**	**.780**	*.004*	**.298**	**.642**	**.211**	**.669**	*.005*	*.000*	**.602**		*.000*	*.000*	*.000*	*.000*	*.000*	*.000*	
Eastern glacial region	KTH-15	*.036*	*.000*	*.000*	**.053**	*.000*	*.000*	*.000*	*.000*	*.022*	**.076**	*.000*	*.000*		*.009*	*.003*	*.013*	*.049*	*.000*	
	KTH-16	*.003*	*.000*	*.000*	**.146**	*.000*	*.000*	*.000*	*.000*	**.068**	*.001*	*.000*	*.000*	*.009*		**.994**	*.000*	*.000*	*.000*	
	KTH-17	*.007*	*.000*	*.000*	**.330**	*.001*	*.000*	*.000*	*.000*	**.172**	*.004*	*.000*	*.001*	*.003*	**.994**		*.000*	*.000*	*.000*	
Tributaries draining Devonian-Carboniferous	KTH-10	*.002*	*.000*	*.000*	*.000*	*.000*	*.000*	*.000*	*.000*	*.000*	*.015*	*.000*	*.000*	*.013*	*.000*	*.000*		**.847**	*.000*	
	KTH-11	*.002*	*.000*	*.000*	*.000*	*.000*	*.000*	*.000*	*.000*	*.000*	*.015*	*.000*	*.000*	*.049*	*.000*	*.000*	**.847**		*.000*	
	KTH-14	*.000*	*.000*	*.000*	*.000*	*.000*	*.000*	*.000*	*.000*	*.000*	*.000*	*.000*	*.000*	*.000*	*.000*	*.000*	*.000*	*.000*		

Note: If the $p > 0.05$, the zircon age populations of two samples are regarded to be indistinguishable, whereas *p* values of 0 have virtual certainty of different parent populations. The crystallization ages of Borohoro plutons are from Wang, Shu, et al. (2007).

The bold and italic values in Table 3 just distinguish the value of $p >$ or < 0.05.

the Devonian and Carboniferous strata (Figures 4 and 5). This observation suggests that the Permian-Carboniferous igneous rocks (Borohoro plutons) in the upper reaches are important sources. Moreover, two remarkable provenance shifts at ca. 7 Ma and ca. 3.3–2.5 Ma were recorded (Figures 4 and 5).

5 | DISCUSSION

5.1 | Landscape evolution of the northern Chinese Tian Shan

The provenance results of the detrital zircon U-Pb dating and heavy mineral assemblages were integrated with existing sedimentology data to reconstruct the source-to-sink the relationship between the northern Tian Shan and the flanking basin, to determine a Late Cenozoic topographic evolution model of the northern Tian Shan.

In the Kuitun River drainage basin, field investigations show that the lower Taxihe Formation is dominated by fine-grained deposits, and consists mostly of reddish and brownish mudstone interbedded with sandstone layers (this study; Sun et al., 2004), which is interpreted as deposited in lacustrine and delta environments under humid conditions (Figure 2). This observation indicates a lack of intensive tectonic movement between ca. 8.7 and 7 Ma (Charreau et al., 2009; Lu et al., 2010; Sun et al., 2004). DZ ages and heavy mineral assemblages from sample KTH-9 demonstrate a diversity of provenance at ca. 8.5 Ma (three major DZ peak ages at ca. 285, 308, and 335 Ma; Figure 4a), further supporting the presence of a broad and open drainage area during that period (Figure 6a). This conclusion is consistent with the previous inference that the central Tian Shan was a likely source region of detrital Taxihe Formation materials into the Jingou River (Chen et al., 2012), which is ~130 km east of the Kuitun River. Thus, we infer that the northern Tian Shan, mostly in the western segment, was still at a relatively low elevation during the Middle Miocene.

By ca. 7.0 Ma, the depositional environment shifts can be observed from a delta to a gravelly braided riverine setting (Figures 2 and 3). As a response, the proportions of DZ age data also show a subtle component change between samples of KTH-9 and KTH-8 (Figure 4). Compared to sample KTH-9, the DZ age range of overlying samples narrow slightly, lacking the U-Pb age population of 310–500 Ma, which suggests that the western granitoid region (western glacial regions in Figure 1

) served as a dominant source for the drainage basin at ca. 6.8–3.3 Ma (Figure 4a). This implies the open Miocene lake was broken, probably due to the growth of topographic relief in the Late Miocene (Jolivet et al., 2018; Figure 6b). Though this provenance shift is not supported by heavy mineral assemblages, the Late Miocene tectonic deformation in the northern Tian Shan has also been evidenced by growth strata analysis (Lu et al., 2010, 2015) and low-temperature thermochronology data (Yin et al., 2017).

Changes in sedimentary facies and accumulation rates (Sun et al., 2004; Figure 2a), including thick conglomerate deposits in the Xiyu Formation (Charreau et al., 2009, 2011), characterize the period between ca. 3.3 and 2.5 Ma. These generally imply the intensely increase in the topographic relief and/or climate fluctuation. The higher abundances of the age population at 265–310 Ma and the occurrence of the DZ age population at ca. <265 Ma in the samples KTH-5 and KTH-04 not only imply that the sediments primarily originated from the source rocks in the uppermost reaches, but also reveal a source change from the western granitoid region to the whole granitoid region (including the western and eastern glacial regions in Figure 1) during the Plio-Pleistocene transition. Moreover, the sample KTH-04 contains more 310–360 Ma DZs and hematite than the Late Miocene–Pliocene samples, which indicates there was an increased contribution of the source from Devonian-Carboniferous strata at ca. 2.5 Ma. This is attributed to a temporary increase in characteristic sediment compositions to the reactivation of the (F_m) linked to basin-ward propagation (Figure 6c). The absence of a sedimentary hiatus from the Taxihe to Xiyu formations, as well as the abundance of relatively unstable heavy minerals species, including epidote, hornblende, and pyroxene in the Xiyu Formation, led us to exclude the possibility that 265–310 Ma DZs from the Late Pliocene to Pleistocene samples were reworked from underlying Cenozoic strata (sediment recycling). Moreover, sediment transport along steep mountainous rivers is very fast, and conglomerate deposition generally occurs by debris flow processes (Miall, 2006). Therefore, it is not considered as an erosion-transport-deposition process over million-year timescales that could have been accomplished in the piedmont region under a drier climate with lower precipitation. These observations, coupled with the initial emergence of schist gravel (only developed in Silurian strata in the highlands) in conglomerate beds at ca. 3 Ma (Figure 4c; Sun et al., 2004), suggests the sediments preserved in the Late Pliocene-Pleistocene deposits mostly come from the most upstream sources (Figure 6c), following the occurrence of the high-energy river systems and erosion range expansions.

Stable accumulation of coarse-grained sediments characterizes the sequence after ca. 2.5 Ma. However, higher abundances of 265–310 Ma DZs in samples KTH-03 and KTH-02 suggest the erosional materials from Devonian-Carboniferous strata were extremely limited (Figure 6d). This implies a progressively retrograde basin-ward propagation that leads to gradual flattening of piedmont thrust belts (dominance by Devonian-Carboniferous strata), which leaves a relatively smooth topography in the northern Tian Shan piedmont,

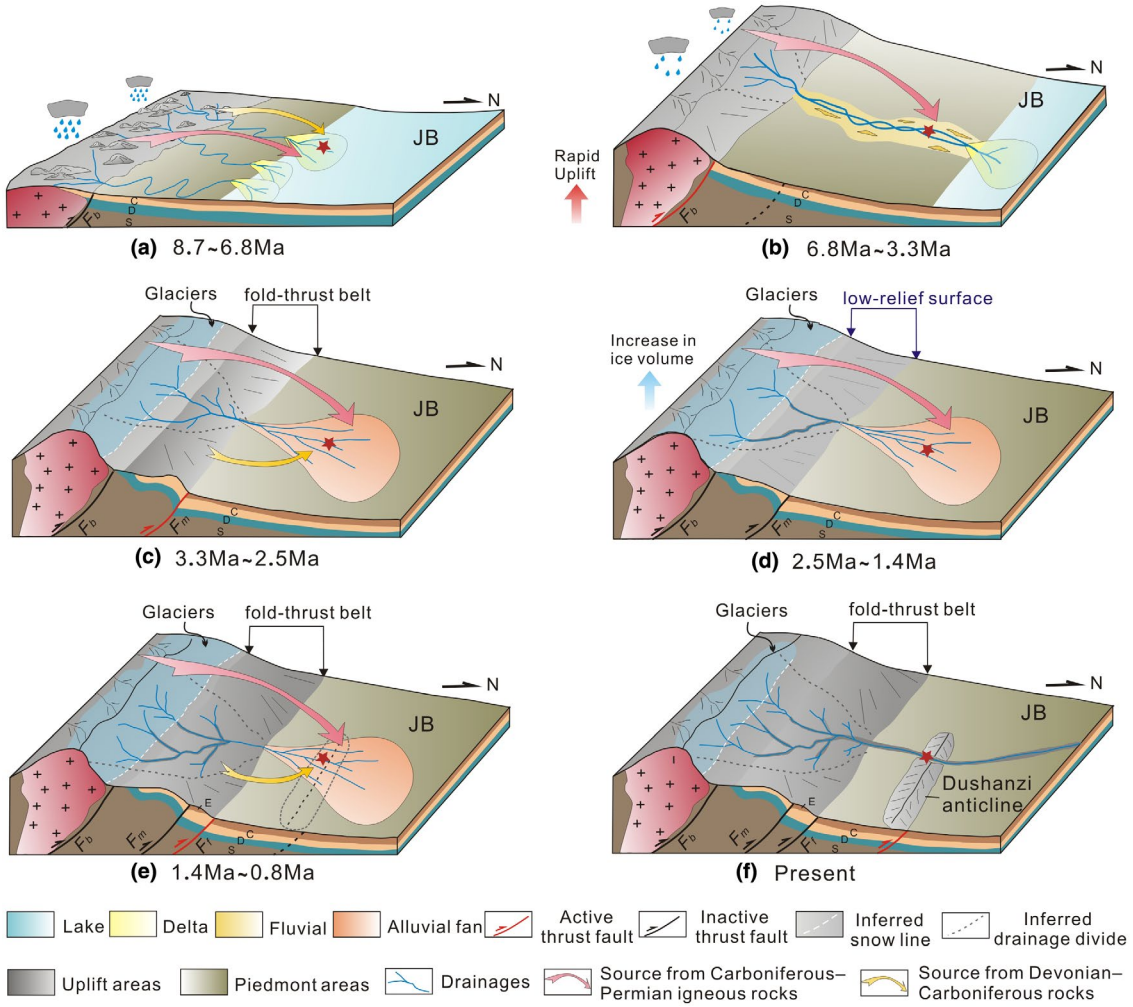

FIGURE 6 Conceptual model of topographic evolution of the northern Tian Shan from the Late Miocene to present. (a) Between8.7 and 6.8Ma, a broad and open drainage area developed, implying a relatively slow tectonic movement. (b) Due to the tectonic reactivation of the pre-Cenozoic fault, the open Miocene lake was broken, evolving towards a braided river system. (c) Glaciation triggered the occurrences of high-energy river systems and erosional expansion at 3.3–2.5 Ma. (d) Enhanced glacial erosion and sediment accumulation within the foreland basin reduced the critical wedge taper and prevented fault propagation. (e) The wedge taper eventually evolved into a supercritical state as faults continued to propagate basin-ward. (f) Neotectonic movement and continuous aridity resulted in a strongly incising riverine system since the Late Pleistocene era. See Section 5 for discussion. JB = Junggar Basin

indicative of a tectonically stable period. After ca. 1.4 Ma, the second-time increase of piedmont source (>310 Ma DZ ages) in sample KTH-01 appears to record the recurrence of fault propagation (Figure 6e).

5.2 | Signature of the tectonic-climatic interaction and its significance

The shifts in the provenance signatures and sedimentary environments are both driven by tectonic activities and/or climatic fluctuations. Previously, the tectonic uplift across the Tianshan Range at ca. 7 Ma had been evidenced by increased sediment accumulation rates and the onset of the syntectonic growth strata in the Jingou River section (Tang, Huang, Dong, Ji, & Ding, 2012), the Chaiwopu Basin (Lu et al., 2015), and the Kuqa foreland basin of the southern Tianshan (Sun et al., 2009), which are concordant with the activation of the Huoerguos-Manas-Tugulu fold-and-thrust belt in the foreland range (Lu et al., 2010, 2019). Additionally, thermochronological data and sedimentary records from the Northern Tibetan Plateau and surrounding areas provided regional evidence for the occurrence of rapid orogenic uplift during the Late Miocene (Sun et al., 2020). Hence, a possible tectonic driver is most likely responsible for the change in sediment supply at ca. 7 Ma. Because tectonic deformation can induce increased topographic gradients, it shrinks the scale of drainage basins; while coarser-grained deposits habitually occur in smaller and steeper catchments (Rickenbach & Koschni, 2010). From a climatological perspective, we also acknowledge increased precipitation can also enhance surface erosion, leading to the increased deposition of coarse-grained

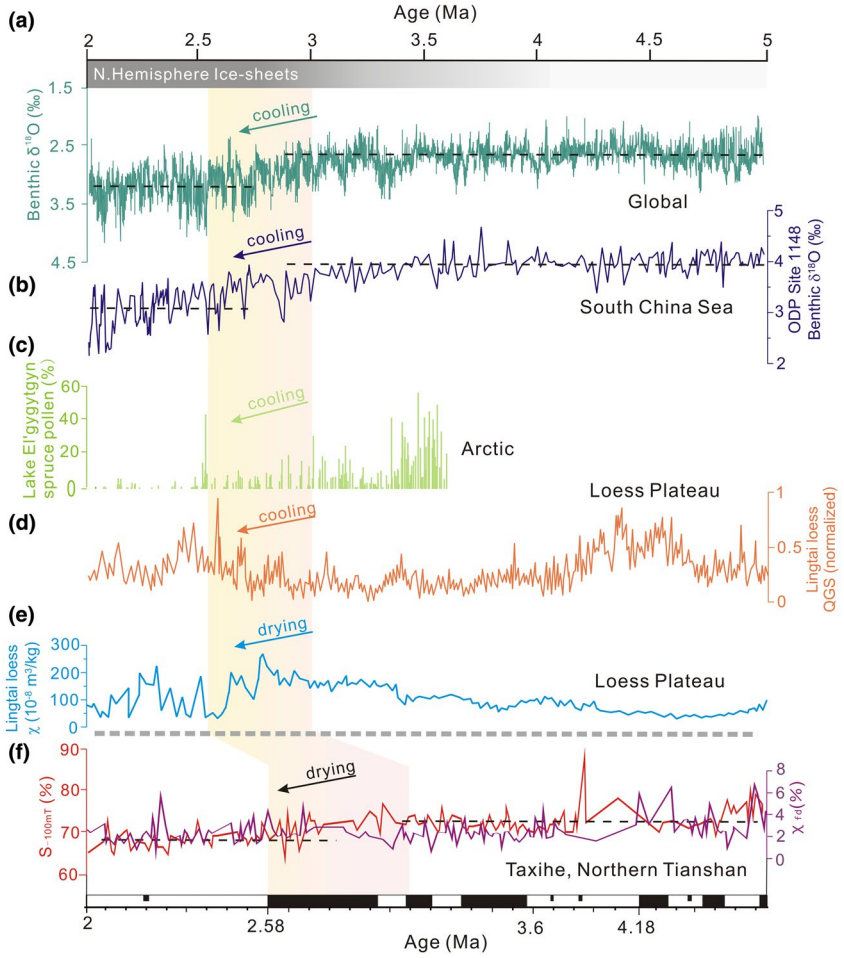

FIGURE 7 Marine and terrestrial records of climate change from 5 to 2 Ma. (a) Benthic δ^{18} O record of global climate variability (Zachos et al., 2008). (b) Benthic δ^{18} O record from the northern South China Sea (Tian, Zhao, Wang, Li, & Cheng, 2008). (c) Pollen record in the Lake El'gygytgyn, Arctic region (Brigham-Grette et al., 2013). (d), (e) Magnetic susceptibility (χ) and quartz grain size (QGS) records from the Lingtai section, Chinese Loess Plateau (Sun et al., 2010). (f) Frequency-dependent magnetic susceptibility (χ_{fd} %) and S_{-100mT} ratio records from the Taxihe section, Northern Chinese Tian Shan (Lu et al., 2013). Associated interpretations of climate change are also from corresponding references

sediments and formation of a high-energy drainage system related to a primary climate driver. However, Sun, Xu, and Huang (2007) showed that steppe taxa obtained from the Dushanzi section were generally dominant from the late Miocene to Pliocene, implying a consistently arid climate during that period; this is inconsistent with the scenario. Based on the previous analysis, it is concluded that the changes in sedimentary environment and provenance in the Dushanzi section at ca. 7 Ma (Figures 2 and 4) is strong direct evidence for tectonic reactivation of Northern Tianshan in the Late Miocene.

As mentioned in Section 5.1, the appearance of the piedmont source at ca. 2.5 Ma probably responded to the recurrence of fault propagation (Figure 4a). Considering this phase of rapid uplift was also broadly reported in northwestern China and the Tibetan Plateau (Deng et al., 2012; Pang et al., 2019; Wang, Zhang, Fang, Dai, & Kempf, 2008), tectonic forces canthus be regarded as the primary cause for the robust sediment supply shift between ca. 3.3 and 2.5 Ma. However, a detailed analysis of provenance indicates the denudation materials within the foreland basin were mainly from the hinterlands of northern Tian Shan (the present-day glacier-covered regions), rather than the piedmont thrust-fold belt. This is not consistent with the tectonosedimentary evolution model of an intracontinental foreland basin (Fang et al., 2016). Specifically, if tectonic deformation was the most important factor controlling sediment transport processes, the Devonian-Carboniferous rocks would be a prominent source of detrital material for the Kuitun River drainage basin, and >310 Ma zircon U-Pb age populations would be expected. However, the study data did not agree with this hypothesis (Figure 4a). In addition, no clear unconformity surface and growth strata were identified in the Pliocene to Pleistocene sequences of the Kuitun River drainage area (Figure 2a). This provenance shift is therefore unlikely to have been primarily controlled by tectonic forces; instead, some climatic factors probably played a key role in controlling the change in sediment transport processes.

The increase in sediment accumulation and transport usually requires higher discharge along the river channel (Strecker et al., 2007). However, previous studies demonstrated that while the Late Pliocene-Pleistocene fluvial-lacustrine sedimentary sequences were deposited, the dominant environments were in an arid phase in the northern Tian Shan foreland basin (Figure 7; Lu et al., 2013). In tectonically active regions with arid climatic conditions, where runoff is ephemeral and flashy, sedimentation may be dominated by rare, violent, and proximal debris flows (Schlunegger

et al., 2017). This is in stark contrast to the results of detailed sedimentological and provenance analyses from the Xiyu Formation, which indicate that sediment transport and deposition were dominated by the sheet flow or stream flow processes where runoff was most likely perennial, and the conglomerate debris was mainly sourced from the most upstream sources.

However, synchronous with the acceleration of detrital supply rates during the Pliocene-Pleistocene period, global climate cooling led to the onset and rapid expansion of the Northern Hemisphere ice-sheets (Figure 7; Zachos, Dichens, & Zeebe, 2008). In glacier-covered regions, glaciation is presumed to have increased orogen denudation rates, and significantly controlled mountain topography, including relief and mean elevation (Berger et al., 2008; Thomson et al., 2010; Whipple, 2009; Zhang et al., 2016). Especially, the initial erosion pulse had a significant transient landscape adjustment to the introduction of efficient glacial erosion (Lease, 2018). Though the effect of glacial erosion within the northern Tian Shan prior to the Late Quaternary is unclear, the provenance shift at ca. 3.3–2.5 Ma was more likely a consequence of the onset and expansion of the Northern Hemisphere ice-sheets, and increased glacial erosion (Charreau et al., 2011; Zhang et al., 2001). This inference is evidenced by the predominance of highlands source signatures during that period (Figure 6c), and is consistent with a temporary increase in ^{10}Be-based paleo-erosion rates at ca. 2.5 Ma from the Kuitun River (Charreau et al., 2011). The PCA plot and MDS diagram (Figure 5) also show that the four samples from the Xiyu Formation are surrounded by source samples from the uppermost reaches of the Kuitun River. Considering the hypothesis that glacial erosion could be more effective than fluvial erosion (Montgomery, 2002), it is reasonable to speculate that the source region expansion at ca. 3–2.5 Ma was probably caused by glacial erosion, thereby leading to increased erosion of fresh detritus, including the eastern granitoid region, and Silurian strata in the source areas. Though glaciation may result in quick mountain erosion, the accumulation of km-thick alluvial fan successions implies that these glaciogenic detritus were transported and deposited by secondary sheet flow or stream flows processes, as were also observed for Holocene fluvioglacial sediments in the Qilianshan area (Hu et al., 2014, 2016). While tectonic deformation or uplift steadily continued within the northern Tian Shan during the Late Pliocene-Pleistocene (Deng et al., 2000; Sun et al., 2004; this study), the tectonic drivers of sediment supply to foreland basin were probably overridden by glaciations induced by global cooling.

This study provides empirical support for the argument that the climate factor has a nonnegligible impact on the process of mountain building (Berger et al., 2008; Cheng et al., 2019; Thomson et al., 2010). Given the explanation in Section 5.1, it is inferred that the Early Pleistocene growth of the northern Tian Shan might obey critical-taper wedge theory. Strong glacial erosion and sedimentation into the foreland basin reduced the critical wedge taper and stabilized piedmont structures by load-induced normal stress, which blocked the continuation of fault propagation (Figure 6d). Decreased erosion rates (Charreau et al., 2011), coupled with continuous internal deformation in northern Tian Shan (Lu et al., 2010) induced the wedge taper to a supercritical state that caused the wedge to propagate basin-ward at ca. 1.4 Ma (Figure 6e). If this was the case, the provenance analysis in this study highlights that climatic driving forces, especially glacial erosion, in central Asia could have a significant effect on the sediment production and landscape evolution of the northern Tian Shan during the Quaternary.

5.3 | Insights into the global Plio-Pleistocene conglomerate origin

Tectonics and climate are generally considered as major controls on regional erosion rate and deposition regimes of terrigenous materials, however, distinguishing the origin mechanism of detritus remains a challenge in some cases. For example, most ancient glaciogenic deposits formed by the dispersal and redeposition of glaciogenic materials through a wide variety of non-glacial processes in almost every conceivable environment (Dreimanis, 1985; Miall, 2016), which generally obscured or covered the primary evidence of its glacial origins. Globally, there is considerable debate around the driving forces of the Late Pliocene-Pleistocene conglomerates along the piedmont (Kong, Zheng, & Fu, 2011; Zhang et al., 2001; Zhao et al., 2017). As represented by the Xiyu conglomerate, Charreau et al. (2009) summarized and analyzed several magnetostratigraphic studies conducted around the Tianshan. They found that the onset of deposition of the Xiyu conglomerates was diachronous and that they were systematically younger towards the basin. Thus, they argued that the Xiyu Formation was a prograding gravel wedge that prograded over the under thrusting forelands, which was primarily controlled by tectonics. However, provenance analysis in this study shows that the Late Pliocene-Pleistocene sediments were derived mainly from the uppermost reaches of the Kuitun River catchment, rather than the middle reaches or emerging structures in the piedmont. Moreover, these magnetostratigraphic sections that constrain the depositional age of the Xiyu-type conglomerates are often far apart, located in different drainage basins around the Tianshan (Charreau et al., 2009), which ignored the impact of the complexity and spatial heterogeneity of climate and tectonic setting on the sedimentary processes.

This study concurs that the deposition of the Miocene Xiyu-like conglomerates around the major mountain ranges in central Asia was related to a primary tectonics driver (Wei

et al., 2018), however, it is also crucial to recognize the prominent contribution of the Plio-Pleistocene climatic transition to the contemporaneous conglomerate deposition. The Plio-Pleistocene transition was characterized by the wide-spread occurrence of coarse clastic deposits along the piedmont of the orogenic belt (Figure 1a; Zhang et al., 2001), such as the Qigequan Formation in the Qaidam Basin (Heermance et al., 2013), the Dayi conglomerate in the Sichuan Basin (Kong et al., 2011), the Yumen conglomerate, and the Jiuquan conglomerate in the Hexi Basin (Zhao et al., 2017) and the Xiyu conglomerate in the Tarim Basin (Charreau et al., 2009; Figure 1a). Previous studies have proposed that the Late Cenozoic evolution of the mountains around the Tibetan Plateau, and associated basin sedimentation were driven by the intracontinental deformation (Burchfiel et al., 1999; Charreau et al., 2008; Zhao et al., 2017). However, this study found from the Tian Shan supports that the onset of Northern Hemisphere glaciation and its associated variations dominated the erosional pattern and sediment input into the basins (Charreau et al., 2011; Zhang et al., 2001), further indicating that climate change could be a primary driving force for the thick coarse deposits during the Quaternary (Zhang et al., 2001).

In tectonically active regions, such as the Chinese Tian Shan, though long-term orogenesis is governed by the regional tectonic setting (e.g. the far-field effects of the India-Asia collision), local Pliocene-Pleistocene alpine glaciation can strongly affect topographic evolution (e.g. relief, mean elevation), leading to tectonic force that was largely perturbed, even overridden by glacial erosion. Globally, similar tectonics-glaciation (climate) interactions during the process of the Quaternary mountain building have been widely reported, such as the St Elias orogen in southern Alaska (Berger et al., 2008), the Western Alaska Range (Lease, 2018), and the Olympic Mountains (Michel, Glotzbach, Adams, & Stübner, 2018). This study emphasizes the crucial role of glaciation in driving physical erosion and surface processes of tectonically active mountainous ranges in glacier-covered regions and presents an important step toward a better understanding of tectonics-climate interaction in producing topography.

6 | CONCLUSIONS

In this study, new detrital zircon U-Pb geochronology and heavy mineral data, as well as previously published detailed field analysis were integrated to reconstruct the Late Cenozoic evolution of the northern Chinese Tian Shan, and the signatures of the driving sedimentation forces in the foreland basin were investigated. Although there were complications due to the entrainment of multiple sediment source regions along the transport pathway, the Late Miocene to Pleistocene deposits contain clear provenance signals that reflect tectonics-climate interaction in regulating landscape evolution according to our interpretations:

1. It is suggested that the northern Tian Shan, at least in the western segment, was still at a relatively low elevation during the Middle Miocene. Until ca. 7 Ma, a significant tectonic event in the Tianshan Range was most likely responsible for the formation of a localized source-to-sink system in the Kuitun River catchment.
2. The Late Pliocene-Pleistocene sediments were mainly derived from the uppermost reaches of the Kuitun River catchment, rather than the middle reaches or emerging structures in the piedmont. This indicates that a shift in sediment supply at 3.3–2.5 Ma could be induced by the onset of the Northern Hemisphere glaciation, leading to the occurrence of a high-energy river system and erosion range expansion.
3. The author's observation that the growth of the northern Tian Shan during the Early Pleistocene might obey critical-taper wedge theory highlights the crucial role of glaciation in driving physical erosion and surface processes in tectonically active mountainous ranges.

ACKNOWLEDGEMENTS

This work was supported by the Second Tibetan Plateau Scientific Expedition and Research (STEP; 2019QZKK0704), the NSF of China (No. 41622204; 41761144071). We gratefully acknowledge the executive editor Dr. Craig Magee, two reviewers Prof. Olivier Dauteuil and Dr. Feng Cheng for their critical and careful reviews, which led to much improvement of this manuscript. We also thank Prof. Weitao Wang and Dr. Gang Hu for constructive suggestions.

DATA AVAILABILITY STATEMENT

The data are used in this paper can be obtained from the fig share website (available from https://figshare.com/s/6c3bbddb3a93a5239a7d).

ORCID

Huiping Zhang https://orcid.org/0000-0002-3042-4301

REFERENCES

Andersen, T. (2002). Correction of common lead in U-Pb analyses that do not report 204Pb. *Chemical Geology*, *192*(1–2), 59–79. https://doi.org/10.1016/S0009-2541(02)00195-X

Angela, M. H., Jacob, A. C., Daniel, F. S., & Andrea, F. (2018). Late Cenozoic cooling favored glacial over tectonic controls on sediment supply to the western Gulf of Mexico. *Geology*, *46*(11), 995–998. https://doi.org/10.1130/G45528.1

Berger, A. L., Gulick, S. P. S., Spotila, J. A., Upton, P., Jaeger, J. M., Chapman, J. B., … McAleer, R. J. (2008). Quaternary tectonic response to intensified glacial erosion in an orogenic wedge. *Nature Geoscience*, *1*(11), 793–799. https://doi.org/10.1038/ngeo334

Brigham-Grette, J., Melles, M., Minyuk, P., Andreev, A., Tarasov, P., DeConto, R., … Herzschuh, U. (2013). Pliocene warmth, polar amplification, and stepped pleistocene cooling recorded in NE Arctic Russia. *Science*, *340*, 1421–1427. https://doi.org/10.1126/science.1233137

Burchfiel, B. C., Brown, E. T., Deng, Q., Li, J., Feng, X., Molnar, P., … You, H. (1999). Crustal shortening on the margins of the Tian Shan: Xinjiang, China. *International Geology Review*, *41*(8), 663–700. https://doi.org/10.1080/00206819909465164

Charreau, J., Avouac, J. P., Chen, Y., Dominguez, S., & Gilder, S. (2008). Miocene to present kinematics of fault-bend folding across the Huerguosi anticline, northern Tianshan (China), derived from structural, seismic, and magnetostratigraphic data. *Geology*, *36*(11), 871–874. https://doi.org/10.1130/G25073A.1

Charreau, J., Blard, P.-H., Puchol, N., Avouac, J.-P., Lallier-Vergès, E., Bourlès, D., … Roy, P. (2011). Paleo-erosion rates in central asia since 9 Ma: A transient increase at the onset of Quaternary glaciations? *Earth and Planetary Science Letters*, *304*(1–2), https://doi.org/10.1016/j.epsl.2011.01.018

Charreau, J., Chen, Y., Gilder, S., Dominguez, S., Avouac, J. P., Sevket, S., … Wang, W. M. (2005). Magnetostratigraphy and rock magnetism of the Neogene Kuitun He section (northwest China): Implications for Late Cenozoic uplift of the Tianshan mountains. *Earth and Planetary Science Letters*, *230*, 177–192. https://doi.org/10.1016/j.epsl.2004.11.002

Charreau, J., Gumiaux, C., Avouac, J. P., Augier, R., Chen, Y., Barrier, L., … Wang, Q. (2009). The Neogene Xiyu Formation, a diachronous prograding gravel wedge at front of the Tianshan: Climatic and tectonic implications. *Earth and Planetary Science Letters.*, *287*, 283–310. https://doi.org/10.1016/j.epsl.2009.07.035

Chen, Y., Fang, X. M., Song, C. H., & Meng, Q. Q. (2012). The uplift and erosion of the Tianshan Mountains recorded by detrital zircon geochronology from the Cenozoic sediments in the southern Junggar Basin. *Earth Science Frontiers*, *19*, 225–233. (in Chinese with English abstract). Retrieved from: http://www.earthsciencefrontiers.net.cn/CN/

Cheng, F., Garzione, C. N., Mitra, G., Jolivet, M., Guo, G. Z., Lu, H. Y., … Wang, L. (2019). The interplay between climate and tectonics during the upward and outward growth of the Qilian Shan orogenic wedge, northern Tibetan Plateau. *Earth-Science Reviews*, *198*, 102945. https://doi.org/10.1016/j.earscirev.2019.102945

Dadson, S. J., Hovius, N., Chen, H., Dade, W. B., Hsieh, M. L., Willett, S. D., … Lin, J. C. (2003). Links between erosion, runoff variability and seismicity in the Taiwan orogen. *Nature*, *426*, 648–651. https://doi.org/10.1038/nature02150

DeCelles, P. G., & Mitra, G. (1995). History of the Sevier orogenic wedge in terms of critical taper models, northeast Utah and southwest Wyoming. *Geological Society of America Bulletin*. *107*(4), 454–462. https://doi.org/10.1130/0016-7606(1995)107<0454:HOTSOW>2.3.CO;2

Deng, Q. D., Feng, X. Y., Zhang, P. Z., Xu, X. W., Yang, X. P., Peng, S. Z., & Li, J. (2000). *Active Tectonics of the Tian Shan Mountains* (in Chinese) (p. 399). Beijing: Seismology Press.

Deng, T., Li, Q., Tseng, Z. J., Takeuchi, G. T., Wang, Y., Xie, G. P., … Wang, X. M. (2012). Locomotive implication of a Pliocene three-toed horse skeleton from Tibet and its paleo-altimetry significance. *Proceedings of National Academy of Sciences of the United States of America*, *109*, 7374–7378. https://doi.org/10.1073/pnas.1201052109

Dreimanis, A., & Schlüchter, C. (1985). Field criteria for the recognition of till or tillite: Palaeogeography. *Palaeoclimatology, Palaeoecology*, *51*, 7–14. https://doi.org/10.1016/0031-0182(85)90079-3

Fang, S. H., Guo, Z. J., Jia, C. Z., Zhang, Z. C., Wang, X. L., & Wang, M. N. (2006). Meso-Cenozoic heavy minerals assemblages in the southern Junggar basin and its implications for basin-orogem pattern. *Chinese Journal of Geology*, 4, 648–662 (in Chinese with English abstract). Retrieved form: http://www.dzkx.org/CN/abstract/abstract9306.shtml

Fang, X., Wang, J., Zhang, W., Zan, J., Song, C., Yan, M., … Lu, Y. (2016). Tectonosedimentary evolution model of an intracontinental flexural (foreland) basin for paleoclimatic research. *Global and Planetary Change*, *145*, 78–97. https://doi.org/10.1016/j.gloplacha.2016.08.015

Gehrels, G., Kapp, P., DeCelles, P., Pullen, A., Blakey, R., Weislogel, A., … Yin, A. (2011). Detrital zircon geochronology of pre-Tertiary strata in the Tibetan-Himalayan orogen. *Tectonics*, *30*, TC5016. https://doi.org/10.1029/2011TC002868

Gillespie, J., Glorie, S., Jepson, G., Zhang, Z. Y., Xiao, W. J., Danišik, M., & Collins, A. S. (2017). Differential exhumation and crustal tilting in the easternmost Tianshan (Xinjiang, China), revealed by low-temperature thermochronology. *Tectonics*, *36*, 2142–2158. https://doi.org/10.1002/2017TC004574

Hammer, Ø., Harper, D. A. T., & Ryan, P. (2001). PAST: Paleontological statistics software package for education and data analysis. *Palaeonotologia Electronica*, *4*, 9. https://palaeo-electronica.org/2001_1/past/issue1_01.htm

Han, B. F., Guo, Z. J., Zhang, Z. C., Zhang, L., Chen, J. F., & Song, B. (2010). Age, geochemistry, and tectonic implications of a late Paleozoic stitching pluton in the North Tian Shan suture zone, western China. *Geological Society of America Bulletin*, *122*(3–4), 627–640. https://doi.org/10.1130/B26491.1

Heermance, R. V., Pullen, A., Kapp, P., Garzione, C. N., Bogue, S., Ding, L., & Song, P. P. (2013). Climatic and tectonic controls on sedimentation and erosion during the Pliocene-Quaternary in the Qaidam basin (China). *Geological Society of America Bulletin*, *125*(5–6), 833–856. https://doi.org/10.1130/B30748.1

Hendrix, M. S., Dumitru, T. A., & Graham, A. S. (1994). Late Oligocene–early Miocene unroofing in the Chinese Tian Shan: An early effect of the India-Asia collision. *Geology*, *22*, 487–490. https://doi.org/10.1130/0091-7613

Herman, F., Seward, D., Valla, P. G., Carter, A., Kohn, B., Willett, S. D., & Ehlers, T. A. (2013). World-wide acceleration of mountain erosion under a cooling climate. *Nature*, *504*, 423–426. https://doi.org/10.1038/nature12877

Hoskin, P., & Black, L. (2000). Metamorphic zircon formation by solid-state recrystallization of protolith igneous zircon. *Journal of Metamorphic Geology*, *18*, 423–439. https://doi.org/10.1046/j.1525-1314.2000.00266.x

Hu, G., Yi, C. L., Zhang, J. F., Liu, J. H., Jiang, T., & Li, S. H. (2016). Late quaternary glacial advances in the eastern Qilianshan, North-Eastern Tibet, as inferred from luminescence dating of fluvioglacial sediments. *Journal of Quaternary Science*, *31*(6), 587–597. https://doi.org/10.1002/jqs.2882

Hu, G., Yi, C. L., Zhang, J. F., Liu, J. H., Jiang, T., & Qin, X. (2014). Optically stimulated luminescence dating of a moraine and a terrace in Laohugou valley, western Qilian Shan, northeastern tibet. *Quaternary International*, *321*, 37–49. https://doi.org/10.1016/j.quaint.2013.12.019

Jolivet, M., Barrier, L., Dauteuil, O., Laborde, A., Li, Q., Reichenbacher, B., … Guo, Z. J. (2018). Late Cretaceous-Palaeogene topography of the Chinese Tian Shan: New insights from geomorphology and sedimentology. *Earth and Planetary Science Letters*, *49*, 95–106. https://doi.org/10.1016/j.epsl.2018.07.004

Kong, P., Zheng, Y., & Fu, B. H. (2011). Cosmogenic nuclide burial ages and provenance of Late Cenozoic deposits in the Sichuan Basin: Implications for Early Quaternary glaciations in east Tibet. *Quaternary Geochronology*, *6*(3–4), 304–312. https://doi.org/10.1016/j.quageo.2011.03.006

Lease, O. R. (2018). Pliocene erosional pulse and glacier-landscape feedbacks in the western Alaska Range. *Earth and Planetary Science Letters*, *497*, 62–68. https://doi.org/10.1016/j.epsl.2018.06.009

Li, J. J., Zhou, S. Z., & Pan, B. T. (1991). The problems of Quaternary glaciation in the eastern part of Qinghai-Xizang plateau. *Quaternary Sciences*, *11*(3), 193–203 (in Chinese with English abstract). Retrieved from: http://www.dsjyj.com.cn/CN/

Litty, C., Lanari, P., Burn, M., & Schlunegger, F. (2017). Climate-controlled shifts in sediment provenance inferred from detrital zircon ages, western Peruvian Andes. *Geology*, *45*(1), 59–62. https://doi.org/10.1130/G38371.1

Lu, H. H., Burbank, D. W., Li, Y. L., & Liu, Y. M. (2010). Late Cenozoic structural and stratigraphic evolution of the northern Chinese Tian Shan foreland. *Basin Research*, *22*, 249–269. https://doi.org/10.1111/j.1365-2117.2009.00412.x

Lu, H. H., Li, B. J., Wu, D. Y., Zhao, J. X., Zheng, X. M., Xiong, J. G., & Li, Y. L. (2019). Spatiotemporal patterns of the Late Quaternary deformation across the northern Chinese Tian Shan foreland. *Earth-Science Reviews*, *194*, 19–37. https://doi.org/10.1016/j.earscirev.2019.04.026

Lu, H. H., Wang, Z., Zhang, T. Q., Zhao, J. X., Zheng, X. M., & Li, Y. L. (2015). Latest Miocene to Quaternary deformation in the southern Chaiwopu Basin, northern Chinese Tian Shan foreland. *Journal of Geophysical Research: Solid Earth.*, *120*(12), 8656–8671. https://doi.org/10.1002/2015JB012135

Lu, H. H., Zhang, W. G., Li, Y. L., Dong, C. Y., Zhang, T. Q., Zhou, Z. Y., & Zheng, X. M. (2013). Rock magnetic properties and paleoenvironmental implications of an 8-Ma late cenozoic Terrigenous succession from the northern Tian Shan foreland basin, northwestern China. *Global & Planetary Change*, *111*, 43–56. https://doi.org/10.1016/j.gloplacha.2013.08.007

Miall, A. D. (1996). *The Geology of Fluvial Deposits: Sedimentary Facies, Basin Analysis, and Petroleum Geology* (pp. 582–584). Berlin: Springer.

Miall, A. D. (2006). *The Geology of Fluvial Deposits: Sedimentary Facies, Basin Analysis, and Petroleum Geology* (pp. 99–130). Berlin: Springer.

Miall, A. D. (2016). *Stratigraphy: A Modern Synthesis*. Switzerland: Springer International Publishing.

Michel, L., Ehlers, T., Glotzbach, C., Adams, B., & Stübner, K. (2018). Tectonic and glacial contributions to focused exhumation in the Olympic Mountains, Washington, USA. *Geology*, *46*(6), 491–494. https://doi.org/10.1130/G39881.1

Molnar, P. (2004). Late Cenozoic increase in accumulation rates of terrestrial sediment: How might climate change have affected erosion rates? *Annual Review of Earth and Planetary Sciences*, *32*, 67–89. https://doi.org/10.1146/annurev.earth.32.091003.143456

Montgomery, D. R. (2002). Valley formation by fluvial and glacial erosion. *Geology*, *30*, 1047–1050. https://doi.org/10.1130/0091

Morton, A. C., & Hallsworth, C. (2007). Stability of detrital heavy minerals during burial diagenesis. In M. A. Mange, & D. T. Wright (Eds.), *Heavy Minerals in Use, Developments in Sedimentology Series* (Vol. *58*, pp. 215–245). Amsterdam, The Netherlands: Elsevier. https://doi.org/10.1016/S0070-4571(07)58007-6

Pang, J. Z., Yu, J. X., Zheng, D. W., Wang, W. T., Ma, Y., Wang, Y. Z., … Wang, Y. (2019). Neogene expansion of the Qilian Shan, north Tibet: Implications for the dynamic evolution of the Tibetan Plateau. *Tectonics*, *38*(3), 1018–1032. https://doi.org/10.1029/2018TC005258

Pfeffer, W. T., Arendt, A. A., Bliss, A., Bolch, T., Cogley, J. G., Gardner, A. S., … Sharp, M. J. (2014). The randolph glacier inventory: A globally complete inventory of glaciers. *Journal of Glaciology*, *60*(221), 537–552. https://doi.org/10.3189/2014JoG13J176

Rickenbach, D., & Koschni, A. (2010). Sediment loads due to fluvial and debris flows during the 2005 flood events in Switzerland. *Hydrological Process*, *24*, 993–1007. https://doi.org/10.1002/hyp.7536

RSGXJR (Regional stratigraphic table compilation group of Xinjiang Uygur Autonomous Region), (1981). *Regional stratigraphic table of Northwest China* (pp. 74–76). Beijing: Geological Publishing House.

Schlunegger, F., Norton, K. P., Delunel, R., Ehlers, T. A., & Madella, A. (2017). Late miocene increase in precipitation in the western cordillera of the andes between 18–19°s latitudes inferred from shifts in sedimentation patterns. *Earth and Planetary Science Letters*, *462*, 157–168. https://doi.org/10.1016/j.epsl.2017.01.002

Searle, M., Avouac, J. P., Elliott, J., & Dyck, B. (2017). Ductile shearing to brittle thrusting along the Nepal Himalaya: Linking Miocene channel flow and critical wedge tectonics to 25th April 2015 Gorkha earthquake. *Tectonophysics*, *714–715*, 117–124. https://doi.org/10.1016/j.tecto.2016.08.003

Sircombe, K. N. (1999). Tracing provenance through the isotope ages of littoral and sedimentary detrital zircon, eastern Australia. *Sedimentary Geology*, *124*(1–4), 47–67. https://doi.org/10.1016/S0037-0738(98)00120-1

Sobel, E., Chen, J., & Heermance, R. V. (2006). Late Oligocene-Early Miocene initiation of shortening in the Southwestern Chinese Tian Shan: Implications for Neogene shortening rate variations. *Earth and Planetary Science Letters*, *247*, 70–81. https://doi.org/10.1016/j.epsl.2006.03.048

Strecker, M. R., Alonso, R. N., Bookhagen, B., Carrapa, B., Hilley, G. E., Sobel, E. R., & Trauth, M. H. (2007). Tectonics and climate of the southern central Andes. *Annual Review of Earth and Planetary Sciences*, *35*, 747–787. https://doi.org/10.1146/annurev.earth.35.031306.140158

Sun, J. M., Li, Y., Zhang, Z. Q., & Fu, B. H. (2009). Magnetostratigraphic data on neogene growth folding in the foreland basin of the southern tianshan mountains. *Geology*, *37*(11), 1051–1054. https://doi.org/10.1130/G30278A.1

Sun, J. M., Xu, Q. H., & Huang, B. C. (2007). Late Cenozoic magnetochronology and paleoenvironmental changes in the northern foreland basin of the Tian Shan Mountains. *Journal of Geophysical Research: Solid Earth*, *112*, B04107. https://doi.org/10.1029/2006JB004653

Sun, J. M., Zhu, R. X., & Bowler, J. (2004). Timing of the Tianshan Mountains uplift constrained by magnetostratigraphic analysis of molasse deposits. *Earth and Planetary Science Letters*, *219*, 239–253. https://doi.org/10.1016/S0012-821X(04)00008-1

Sun, Y., An, Z., Clemens, S. C., Bloemendal, J., & Vandenberghe, J. (2010). Seven million years of wind and precipitation variability on the Chinese Loess Plateau. *Earth and Planetary Sciences Letter*, *297*(3–4), 525–535.

Sun, Y. B., Yan, Y., Nie, J. S., Li, G. J., Shi, Z. G., Qiang, X. K., … An, Z. S. (2020). Source-to-sink fluctuations of Asian aeolian deposits since the late Oligocene. *Earth-Science Reviews*, *200*, 102963. https://doi.org/10.1016/j.earscirev.2019.102963

Tang, Z. H., Huang, B. C., Dong, X. X., Ji, J. L., & Ding, Z. L. (2012). Anisotropy of magnetic susceptibility of the Jingou River section: Implications for late Cenozoic uplift of the Tian Shan. *Geochemistry Geophysics Geosystems*, *13*(3), https://doi.org/10.1029/2011GC003966

Thomson, S. N., Brandon, M. T., Tomkin, J. H., Reiners, P. W., Vásquez, C., & Wilson, N. J. (2010). Glaciation as a destructive and constructive control on mountain building. *Nature*, *7313*(467), 313–317. https://doi.org/10.1038/nature09365

Tian, J., Zhao, Q. H., Wang, P. X., Li, Q. Y., & Cheng, X. R. (2008). Astronomically modulated Neogene sediment records from the South China Sea. *Paleoceanography*. *23*, PA3210. https://doi.org/10.1029/2007PA001552

Vermeesch, P. (2013). Multi-sample comparison of detrital age distributions. *Chemical Geology*, *341*, 140–146. https://doi.org/10.1016/j.chemgeo.2013.01.010

Wang, B., Shu, L. S., Cluzel, D., Faure, M., & Charvet, J. (2007). Geochronological and geochemical studies on the Borohoroplutons, north of Yili, NW Tianshan and their Tectonic implication. *Acta Petrologica Sinica*, *23*(8), 1885–1900.

Wang, Q., Wyman, D. A., Zhao, Z. H., Xu, J. F., Bai, Z. H., Xiong, X. L., … Chu, Z. Y. (2007). Petrogenesis of Carboniferous adakites and Nb-enriched arc basalts in the Alataw area, northern Tianshan Range (western China): Implications for Phanerozoic crustal growth in the Central Asia orogenic belt. *Chemical Geology*, *236*, 42–64. https://doi.org/10.1016/j.chemgeo.2006.08.013

Wang, S. F., Zhang, W. L., Fang, X. M., Dai, S., & Kempf, O. (2008). Magnetostratigraphy of the Zanda basin in southwest Tibet Plateau and its tectonic implications. *Chinese Science Bulletin*, *53*, 1393–1400. https://doi.org/10.1007/s11434-008-0132-9

Wang, W. T., Zhang, P. Z., Yu, J. X., Wang, Y., Zheng, D. W., Zheng, W. J., … Pang, J. Z. (2016). Constraints on mountain building in the northeastern Tibet: Detrital zircon records from synorogenic deposits in the Yumen Basin. *Scientific Reports*, *6*(1), 27604. https://doi.org/10.1038/srep27604

Wei, X. C., Zheng, H. B., Wang, P., Tada, R., Clift, P. D., Jourdan, F., … Chen, H. L. (2018). Miocene volcaniclastic sequence within the Xiyu Formation from source to sink: Implications for drainage development and tectonic evolution in eastern Pamir, NW Tibetan Plateau. *Tectonics*, *37*, 3261–3284. https://doi.org/10.1029/2018TC005008

Whipple, K. X. (2009). The influence of climate on the tectonic evolution of mountain belts. *Nature Geoscience*, *2*(2), 97. https://doi.org/10.1038/ngeo413

Windley, B. F., Allen, M. B., Zhang, C., Zhao, Z. Y., & Wang, G. R. (1990). Paleozoic accretion and Cenozoic redeformation of the Chinese Tien Shan Range. *Central Asia. Geology*, *18*(2), 128. https://doi.org/10.1130/0091-7613(1990)018<0128:PAACRO>2.3.CO;2

Xiang, D. F., Zhang, Y. Z., Xiao, W. J., Zhu, W. B., Zheng, D. W., Li, G. W., … Pang, J. Z. (2019). Episodic Meso-Cenozoic denudation of Chinese Tianshan: Evidence from detrital apatite fission track and zircon U-Pb data, southern Junggar Basin margin, NW China. *Journal of Asian Earth Sciences*, *175*, 199–212. https://doi.org/10.1016/j.jseaes.2018.07.042

Yang, Y. T., Song, C. C., & He, S. (2015). Jurassic tectonostratigraphic evolution of the Junggar basin, NW China: A record of Mesozoic intraplate deformation in Central Asia. *Tectonics*, *34*, 86–115. https://doi.org/10.1002/2014TC003640

Yin, A., Dang, Y. Q., Zhang, M., Chen, X. H., & McRivette, M. W. (2008). Cenozoic tectonic evolution of the Qaidam basin and its surrounding regions (Part 3): Structural geology, sedimentation, and regional tectonic reconstruction. *Geological Society of America Bulletin*, *120*(7–8), 847–876. https://doi.org/10.1093/petrology/egl007

Yin, A., Nie, S., Craig, P., Harrison, T. M., Ryerson, F. J., Qian, X. L., & Yang, G. (1998). Late Cenozoic tectonic evolution of the southern Chinese Tian Shan. *Tectonics*, *17*, 1–27. https://doi.org/10.1029/97TC03140

Yin, J. Y., Chen, W., Hodges, K. V., Xiao, W. J., Cai, K. D., Yuan, C., … Soest, M. C. (2017). The thermal evolution of Chinese central Tianshan and its implications: Insights from multi-method chronometry. *Tectonophysics*, *722*(2), 536–548.

Yuan, H. L., Gao, S., Liu, X. M., Li, H. M., Günther, D., & Wu, F. Y. (2004). Accurate U-Pb age and trace element determinations of zircon by laser ablation inductively coupled plasma mass spectrometry. *Geostandards & Geoanalytical Research*, *28*, 335–370. https://doi.org/10.1111/j.1751-908X.2004.tb00755.x

Zachos, J. C., Dichens, G. D., & Zeebe, R. E. (2008). An early Cenozoic perspective on greenhouse warming and carbon-cycle dynamics. *Nature*, *451*, 279–283. https://doi.org/10.1038/nature06588

Zhang, H. Y. (1985). Quaternary glaciation in the northern Tianshan. In: D. H. Mao, Z. X. Yang, C. J. Zhou, J. F. Li, X. C. Xia, S. J. Wang, X. L. Peng, L. Hong, S. T. Han, & H. Y. Zhang (Eds.), *Proceedings of Quaternary Research of Arid Xinjiang* (pp. 55–68). Urumuqi: Xinjiang Renmin Press.

Zhang, H. Z., Lu, H. Y., Stevens, T., Han, F., Fu, Y., Geng, J. Y., & Wang, H. L. (2018). Expansion of dust provenance and aridification of Asia since ~7.2 Ma revealed by detrital zircon U-Pb dating. *Geophysical Research Letters*, *45*(24), 13,437–13,448. https://doi.org/10.1029/2018GL079888

Zhang, H. P., Oskin, E. O., Liu-Zeng, J., Zhang, P. Z., Reiners, P. W., & Xiao, P. (2016). Pulsed exhumation of interior eastern tibet: Implications for relief generation mechanisms and the origin of high-elevation planation surfaces. *Earth and Planetary Science Letters*, *449*, 176–185. https://doi.org/10.1016/j.epsl.2016.05.048

Zhang, P. Z., Molnar, P., & Downs, W. R. (2001). Increased sedimentation rates and grain sizes 2–4 Myr ago due to the influence of climate change on erosion rates. *Nature*, *410*, 891–897. https://doi.org/10.1038/35073504

Zhang, X. R., Zhao, G. C., Sun, M., Paul, R. E., Han, Y. G., Liu, D. X., … Xu, B. (2015). Tectonic evolution from subduction to arc-continent collision of the Junggar ocean: Constraints from U-Pb dating and Hf isotopes of Detrital zircons from the north Tanshan belt, NW China. *Geological Society of America Bulletin*, *128*, 644–660. https://doi.org/10.1130/B31230.1

Zhao, J. D., Liu, S. Y., He, Y. Q., & Song, Y. G. (2009). Quaternary glacial chronology of the Ateaoyinake river valley, Tianshan Mountains, China. *Geomorphology*, *103*, 276–284. https://doi.org/10.1016/j.geomorph.2008.04.014

Zhao, J. D., Zhou, S. Z., He, Y. Q., Ye, Y. G., & Liu, S. Y. (2006). ESR dating of glacial tills and glaciations in the Urumqi river headwaters,

Tianshan Mountains, China. *Quaternary International*, *144*(1), https://doi.org/10.1016/j.quaint.2005.05.013

Zhao, Z. J., Granger, D. E., Chen, Y., Shu, Q., Liu, G. F., Zhang, M. H., … Qiao, L. L. (2017). Cosmogenic nuclide burial dating of an alluvial conglomerate sequence: An example from the Hexi corridor, NE Tibetan Plateau. *Quaternary Geochronology*, *39*, 68–78. https://doi.org/10.1016/j.quageo.2017.02.007

Zhu, Y. F., Zhang, L. F., Gu, L. B., Guo, X., & Zhou, J. (2005). The zircon SHRIMP chronology and trace element geochemistry of the Carboniferous volcanic rocks in western Tianshan Mountains. *Chinese Science Bulletin*, *50*, 2201–2212. https://doi.org/10.1007/BF03182672

SUPPORTING INFORMATION

Additional Supporting Information may be found online in the Supporting Information section.

How to cite this article: Zhao X, Zhang H, Lv H, et al. Signatures of tectonic-climatic interaction during the Late Cenozoic orogenesis along the northern Chinese Tian Shan. *Basin Res*. 2021;33:291–311. https://doi.org/10.1111/bre.12466